

Star formation in Perseus

II. SEDs, classification and lifetimes

J. Hatchell¹, G. A. Fuller², J. S. Richer³, T.J.Harries¹, E. F. Ladd⁴

¹ School of Physics, University of Exeter, Stocker Road, Exeter EX4 4QL, U.K.

² School of Physics & Astronomy, University of Manchester, P.O. Box 88, Manchester M60 1QD, U.K.

³ Cavendish Laboratory, Cambridge CB3 0HE, U.K.

⁴ Department of Physics and Astronomy, Bucknell University, Lewisburg, PA 17837, U.S.A.

ABSTRACT

Context. Hatchell et al. (2005) (Paper I) published a submillimetre continuum map of the Perseus molecular cloud, detecting the starless and protostellar cores within it.

Aims. To determine the evolutionary stage of each submm core in Perseus, and investigate the lifetimes of these phases.

Methods. We compile spectral energy distributions (SEDs) from 2MASS (1–2 μm), Spitzer IRAC (3.6, 4.5, 5.8, 8.0 μm), Michelle (11 and 18 μm), IRAS (12, 25, 60, 100 μm), SCUBA (450 and 850 μm) and Bolocam(1100 μm) data. Sources are classified starless/protostellar on the basis of infrared and/or outflow detections and Class I/Class 0 on the basis of T_{bol} , $L_{\text{bol}}/L_{\text{sun}}$ and $F_{3.6}/F_{850}$. In order to investigate the dependence of these evolutionary indicators on mass, we construct radiative transfer models of Class 0 sources.

Results. Of the submm cores, 56/103 (54%) are confirmed protostars on the basis of infrared emission or molecular outflows. Of these, 22 are classified Class I on the basis of three evolutionary indicators, 34 are Class 0, and the remaining 47 are assumed starless. Perseus contains a much greater fraction of Class 0 sources than either Taurus or Rho Oph. We derive estimates for the correlation between bolometric luminosity and envelope mass for Class I and Class 0 sources.

Conclusions. Comparing the protostellar with the T Tauri population, the lifetime of the protostellar phase in Perseus is 0.25–0.67 Myr (95% confidence limits). The relative lifetime of the Class 0 and Class I phases are similar, confirming the results of Visser et al. (2002) in isolated cores. We find that for the same source geometry but different masses, evolutionary indicators such as T_{bol} vary their value. It is therefore not always appropriate to use a fixed threshold to separate Class 0 and Class I sources. More modelling is required to determine the observational characteristics of the Class 0/Class I boundary over a range of masses.

Key words. Submillimeter; Stars: formation; Stars: evolution; ISM: structure; ISM: dust, extinction

1. Introduction

The submillimetre (submm) surveys of the Perseus molecular cloud with SCUBA (Hatchell et al. 2005, hereafter Paper I) and Bolocam (Enoch et al. 2006) have for the first time produced a fairly complete census of the star formation activity in this cloud, identifying all the submm cores above their flux detection limits. Previously, these submm cores have been discussed in terms of their masses, clustering and their relationship to the molecular cloud (Hatchell et al. 2005; Enoch et al. 2006; Kirk et al. 2006) but so far there has been little attempt to identify their evolutionary status. With an identification of the protostars amongst the ~ 100 submm cores, questions of the star formation rate, the timescales of the prestellar and protostellar phases, and the detailed evolution of protostars can be addressed.

The timescales involved in protostellar formation are particularly important as constraints on the underlying physics controlling the protostellar collapse. If cores form at the point where turbulence rapidly completely dissipates, then collapse should occur on roughly a free-fall time. If, on the other hand, magnetic fields and ambipolar diffusion play an important role in the evolution of the cores, then the time for a core to collapse can be greatly increased (Tassis & Mouschovias 2004). Current estimates for the ratio of the prestellar to the protostellar life-

time vary from 2–3 (Visser et al. 2002; Lee & Myers 1999) to 10 (Ward-Thompson et al. 1994; Jessop & Ward-Thompson 2000).

Estimates for the lifetime of an embedded low-mass protostar are $1\text{--}2 \times 10^5$ Myr (Greene et al. 1994; Kenyon & Hartmann 1995; Wilking et al. 1989; Kenyon et al. 1990). These early estimates were based on infrared surveys (eg. IRAS) with very incomplete counts of protostars. Now that we have a submm-based census of the protostellar counts in Perseus, combined with much more complete estimates of the T Tauri population down to below the brown dwarf limit (Muench et al. 2003; Wilking et al. 2004; Jørgensen et al. 2006), and new age estimates for the T Tauri population using updated pre-main-sequence (PMS) evolutionary tracks (Wilking et al. 2004; Mayne et al. in prep.), it is time to revisit these estimates.

A catalogue of protostellar sources also provides a valuable resource for followup study (eg. with interferometers such as ALMA) as subsamples with particular properties (starless/protostellar, mass, luminosity) can be identified in order to investigate specific aspects of protostellar or starless core evolution.

An established method of differentiating between protostars and starless cores is on the basis of their spectral energy distributions (SEDs). Perseus has now been surveyed not only in the mm/submm by SCUBA and Bolocam but also across the infrared by 2MASS, Spitzer and IRAS, so fluxes are available

across a wide range of wavelengths. Using these publicly available data we can compile a set of spectral energy distributions for the submm sources in Perseus which is based on a homogeneous dataset. These consistent spectral energy distributions are an important tool in determining evolutionary stage.

In this paper we collate the spectral data on the submm sources in Perseus and discuss the evolution and lifetimes of protostars within the cloud. In Sect. 2 we discuss the derivation of fluxes for the SEDs, including the new mid-infrared observations with Michelle on UKIRT, and in Sect. 2.2 the resulting SEDs. Sect 3 discusses the resulting classification and its implications. In Sect 4 we present models of early Class 0 sources and their implications for the classification. In Sect. 5 we consider the lifetime of the embedded protostellar phase and our conclusions are summarised in Sect. 6.

Throughout, we assume a distance of 320 pc for the Perseus molecular cloud based on the Hipparcos distance of IC348 (de Zeeuw et al. 1999), consistent with our earlier paper (Paper I), though other recent studies (Kirk et al. 2006; Enoch et al. 2006) have assumed a closer distance of 250 pc based on extinction studies (Černis & Straizys 2003, and references therein).

2. Spectral energy distributions

We have compiled a spectral energy distribution (SED) for each submm source in Perseus, based on an extended version of the 850 μm catalogue given in Paper I. With a mass limit of 0.1 M_{\odot} for a 30 K protostellar envelope or 0.5 M_{\odot} for a 10 K starless core, the sources we expect to detect in the submm are those at the earliest stages of protostellar evolution – starless, Class 0 and Class I.

2.1. Contributions to the SED

Spectral energy distributions were compiled from fluxes either from images or catalogues from the following datasets: 2MASS (1-2 μm), Spitzer IRAC (3.6, 4.5, 5.8, 8.0 μm), Michelle (11 and 18 μm), IRAS (12, 25, 60, 100 μm), SCUBA (450 and 850 μm , Paper I) and Bolocam (1100 μm , Enoch et al. 2006).

2.1.1. SCUBA 850 μm and master catalogue

SCUBA 850 μm fluxes are taken from our SCUBA map (Hatchell et al. 2005). The JCMT beam size at this wavelength is 14''.

The SCUBA chop results in poor sensitivity and noise artefacts in reconstructed maps on angular scales $\geq 100''$ (see Johnstone et al. 2000; Visser et al. 2002, Fig. 1). To avoid false detections and large uncertainties on measurements of the extended flux we take out the large spatial scales by applying an unsharp mask (USM) filter. This filter removes structure on scales of $> 2'$ (40,000 AU at 320 pc). This was implemented by convolving the map with a 2' FWHM Gaussian and subtracting the resulting smoothed map from the original. This filtering also selects appropriate spatial scales for candidate protostars (eg. Motte et al. 1998).

To find integrated source fluxes for the 850 μm sources we ran Clumpfind (2D version) (Williams et al. 1994) and SExtractor (Bertin & Arnouts 1996) on the SCUBA data from Paper I. Clumpfind allocates pixels (and therefore flux) below the highest closed contour to sources using a friend-of-friends method. We also used SExtractor to extract fluxes within a fixed

90'' aperture. We ran Clumpfind with a base level of 3σ and increments of 1σ ($\sigma = 35$ mJy/beam at 850 μm and 200 mJy/beam at 450 μm) and a minimum pixel count of 5 (3'' pixels).

The catalogue for which we calculate SEDs (the master catalogue) consists of (a) all sources with a peak flux above 5σ at 850 μm and a Clumpfind detection from the SCUBA 850 μm USM map; (b) Clumpfind detections with a peak flux above 3σ at 850 μm and either an identification in Paper I, or a Bolocam 1.1mm detection with Clumpfind (Enoch et al. 2005). We additionally included the well known Class I source IRAS 03410+3152 which is a 3σ 850 μm detection with Clumpfind in this category. The requirement for a Clumpfind detection means that we can allocate 850 μm source integrated fluxes to every source presented here in a consistent way. The 5σ detection limit provides a peak flux limited catalogue. Our aim in the wider compilation including the 3σ sources with multiple detections is to include as many real sources as possible while minimising the number of artefacts.

The requirement of 5 pixels above 3σ with a 5σ peak should include any true point source with a peak above 5σ while ruling out noise spikes. The corresponding point source mass limit at 850 μm is 0.5 M_{\odot} at 10 K. The maximum mass within one beam of a starless core which escapes our detection limit is therefore 0.5 M_{\odot} (see Sect. 2.2.2 for the details of the mass calculation). The masses calculated from flux within the Clumpfind area do not take into account low level flux $< 3\sigma$ outside this area. Where the integrated flux is less than the peak flux per beam, the peak flux per beam is used to calculate masses. This affects 12 low mass sources, mainly Bolocam detections with an 850 μm peak $< 5\sigma$. The lower requirement of 5 pixels above 3σ with a peak of at least 3σ corresponds to a mass of 0.3 M_{\odot} at 10K.

Several further sources which we identified by eye in Paper I were also not identified by Clumpfind as separate sources but merged into one clump. SExtractor 90'' aperture fluxes are also included in the SEDs for comparison with the Clumpfind fluxes to give an idea visually of the uncertainties due to the differing clump extraction methods. The Paper I source numbers (in some cases multiple) corresponding to each Clumpfind source are listed in Table 5 along with the cross-identification from the 2MASS and Bolocam catalogues and other known names for each source. The source positions listed in Table 5 and used for cross-identification with sources at other wavelengths are the positions of peak 850 μm flux. Pointing with SCUBA is typically good to within 3''.

2.1.2. SCUBA 450 μm

SCUBA 450 μm integrated fluxes (beam size 8'') were also taken from our SCUBA maps (Paper I). As for the 850 μm data, 2D Clumpfind was run on the unsharp masked map. Contours were set to 3σ , $3\sigma + 2'' \times 1\sigma$ with $n = 0-6$ and $\sigma = 200$ mJy/beam. For many of the 850 μm sources, no corresponding 450 μm peak was identified largely due to the higher relative noise level on the 450 μm map. The 450 μm fluxes are generally integrated over a smaller area than the 850 μm fluxes due to the higher noise level at this shorter wavelength.

2.1.3. Bolocam

Bolocam 1.1mm fluxes were taken from Enoch et al. (2006) where Bolocam peak positions were within 20'' of the 850 μm peak. The large offset allowed takes account of the compara-

tively large beam of Bolocam (30'' compared to SCUBA's 14''). The median offset between SCUBA and Bolocam peaks was 9''.

2.1.4. IRAS

Upper limits on the IRAS fluxes were taken from HIRES processed maps. The HIRES processing was carried out with 120 iterations at 60 and 100 μ m and 40 at 12 and 25 μ m, following the method used successfully on the L1448 cluster (Wolf-Chase et al. 2000). The resulting beams are typically 50–90'' at 100 μ m and 25–60'' at 12 μ m. Despite the HIRES processing many of the sources are still confused. As the 100 μ m beam sizes are usually large compared to the 850 μ m sources, the FIR flux for each submm core falls within one HIRES beam, and therefore the HIRES peak flux per beam for each source can be used as an estimate of the total flux. There may also be a contribution from nearby neighbours where sources are tightly packed, and for that reason the IRAS HIRES fluxes are marked as upper limits on the SEDs.

2.1.5. Michelle on UKIRT

Observations were carried out using MICHELLE on UKIRT¹ on the nights of 14 September to 21 September 2002. The instrument has a field of view of 67'' by 50'' with 0.21'' pixels. Using 11.6 μ m and 18.5 μ m narrowband filters contiguous regions were imaged to cover the brighter SCUBA submillimetre peaks, concentrating on the regions known to contain clusters: the IC348(HH211), L1448, L1455 and NGC1333 regions. During the observations the seeing had a FWHM of $\sim 0.7''$ at 11.6 μ m and $\sim 1''$ at 18.5 μ m. Source fluxes were measured in 2'' or 2.5'' apertures and the typical 1-sigma noise levels reached in the observations were 30 mJy at 11.6 μ m and between 90 mJy and 200 mJy at 18.5 μ m.

2.1.6. Spitzer IRAC

Spitzer IRAC maps at 3.6, 4.5, 5.8, 8.0 μ m observed as part of the Cores to Disks legacy project (Evans et al. 2003) were extracted from the archive using Leopard. Source positions and fluxes were extracted using SExtractor (Bertin & Arnouts 1996) and source detection was carried out on the median map. Fluxes were measured within isophotal areas down to a threshold of twice the local background, which was typically 0.1–0.2 MJy Sr⁻¹ at 3.6 μ m and 6–15 MJy Sr⁻¹ at 8 μ m. Spitzer sources were considered to be associated with SCUBA sources where they lay within 12'' or the Clumpfind source FWHM, whichever was the larger, of the peak. No preselection was made on Spitzer colours, unlike Jørgensen et al. (2006).

2.1.7. 2MASS

JHK fluxes were taken from the 2MASS point source catalogue for sources with rising (red) spectral indices $H - K > 0.8$ which lay within 12'' or the submm source FWHM (as determined by Clumpfind), whichever was the larger, of the SCUBA 850 μ m peak.

2.2. Results

SEDs for each source are shown in Fig. 7. Every SED includes the 850 μ m flux from Clumpfind, a Bolocam 1100 μ m flux or limit, IRAS HIRES upper limits, and Spitzer IRAC and 2MASS fluxes or upper limits. Additionally, an 850 μ m flux in a 90'' aperture is shown for the majority of sources (those identified by SExtractor), a 450 μ m integrated flux for sources identified by Clumpfind on the 450 μ m map, and Michelle 11.6 and 18.5 μ m fluxes where available. For a few well-known sources further flux constraints are available in the literature but we have not included these as our aim was to compile as homogeneous a dataset as possible. The differing flux extraction methods, in particular the necessarily different areas for flux measurement, result in some mismatches in the SEDs. In a very few cases there are apparent mismatches between a submm source and an infrared source with falling spectrum (sources 12, 13, 58, 62, 65, 70).

2.2.1. T_{bol} and L_{bol}

For each source we calculated the bolometric temperature T_{bol} and bolometric luminosity L_{bol} using a piecewise integration between the flux measurements following Myers & Ladd (1993). Where there is no Spitzer, Michelle or 2MASS detection, both T_{bol} and L_{bol} are taken as upper limits to reflect the fact that the HIRES fluxes are upper limits. The bolometric temperature T_{bol} is robust to calibration uncertainties or missing fluxes with even a factor 2 change between submm and MIR wavebands changing T_{bol} by only a few kelvin. The bolometric luminosities are set largely by the far-infrared limits set by IRAS HIRES, which we estimate in uncrowded regions are good to 30% but in crowded regions may lead to overestimates of the luminosity due to flux contributions from neighbouring sources.

2.2.2. Masses

We calculate envelope masses based on a constant dust temperature of $T_{\text{d}} = 10$ K and a 850 μ m dust opacity of 0.012 cm² g⁻¹. The temperature of 10 K was required by the constraints of the SCUBA 850 μ m and IRAS HIRES 100 μ m fluxes on model greybodies (assuming Ossenkopf & Henning (1994) icy coagulated dust type 5). Even at 10 K 13% of the 100 micron upper limits fall below the prediction of the greybody. Greybodies at $T_{\text{d}} = 10$ K are plotted on the SEDs in Fig.7; note that the 850 micron aperture fluxes (90'' diameter aperture, solid triangles) are often lower than the Clumpfind fluxes and the 450 micron fluxes, which also often fall below the greybody, are calculated over a smaller area. Higher temperatures, even as high as 12 K, were ruled out for the main component of mass in most sources. For comparison, models of Class 0 and Class I sources (Shirley et al. 2002; Young et al. 2003) suggest that the isothermal dust temperature with which to calculate representative masses should be 13.8 ± 2.4 K for Class 0 sources and 16 ± 4 K for Class 1 sources, consistent with 10 K. Temperatures derived from modelling the cores in Perseus as Bonnor-Ebert spheres (Kirk et al. 2006) indicate temperatures between 10–19K. The 10 K to which we are constrained by the greybodies lies at the low end of the expected temperature range, at least for the protostellar sources if not the starless cores. Thus our SEDs point to detection of a larger fraction of cold dust than is often measured for protostars, for which mean dust temperatures of up to 30 K are often assumed when calculating masses from submm fluxes.

¹ The United Kingdom Infrared Telescope (UKIRT) is operated by the Joint Astronomy Centre on behalf of the U.K. Particle Physics and Astronomy Research Council.

A reason for the detection of more cold dust in our sample could be that the submm fluxes are taken from the Clumpfind deconvolution rather than more limited apertures, even though the map was prefiltered to remove structure on scales above $2'$ before running Clumpfind. IRAS HIRES fluxes also provide tighter upper limits on the source fluxes than the IRAS PSC by reducing the contribution from nearby emission. However, the Clumpfind components are no bigger than the IRAS HIRES beam at $100\mu\text{m}$ (typically $80''$) so the SED should give a fair representation of the clump. Considering all the uncertainties in calculating masses, we find that the true masses could be lower than our estimates but are unlikely to be higher. Firstly this is a result of the low T_d compared to studies which assume higher temperatures - a factor of 3 compared to 15 K or 6 compared to 30 K. Secondly, we assume 320 pc whereas 250 pc is also an arguable distance for Perseus (Černis & Straizys 2003), which would reduce masses by a factor 1.9. Note, though, that our masses are consistent with the Bolocam study of Perseus (Enoch et al. 2006), which also assumed 10 K, once their lower assumed distance is taken into account. Our dust opacity of $0.012\text{ cm}^2\text{ g}^{-1}$, taken from Ossenkopf & Henning (1994) assuming a gas/dust ratio of 161 by mass, is also at the low end of the range. Some authors prefer $0.02\text{ cm}^2\text{ g}^{-1}$ at $850\mu\text{m}$, which also would reduce masses by a factor 1.7. In summary, with a different choice of factors and fluxes measured in a more limited aperture, masses could be up to a factor of 10 lower than these we give.

The results for masses along with T_{bol} and L_{bol} are given in Table 4.

3. Classification

The shape of the SED only depends on the dust distribution relative to the heating source and this depends on many parameters – envelope mass, which determines the overall optical depth (Ivezic & Elitzur 1997); clumpiness (Indebetouw et al. 2006); orientation of any outflow cavity (Whitney et al. 2003); and location of heating source on the near or far side of the clump. However, there are well known general trends with evolutionary stage, as the overall envelope mass reduces and the size of the outflow cavity increases (Whitney et al. 2003; Arce & Sargent 2006). Bearing the caveats in mind, we apply a number of evolutionary indicators to classify our objects based on their SEDs. As we are largely interested in statistics, individual misclassifications due to an edge-on or pole-on orientation are less important as to some extent they cancel out across the population as a whole. What is important is that we use a consistent set of measurements across our sample, and therefore can directly compare between sources.

We assume our sources fall into the usual classification scheme of starless core, Class 0 or Class I protostar. Starless cores are those that do not contain a hydrostatic core (though some starless cores are protostellar cores which will go on to form one); observationally they are cold and show no evidence for embedded infrared, radio or outflow sources. The boundary between the two protostellar classes, Class 0 and I, is defined by the point in evolution when the mass of the envelope equals the stellar mass. However, we have no way of measuring the stellar mass and instead must rely on criteria from modelling and/or observation to separate Class 0 and Class I sources based on evolutionary indicators derived from observables.

The first two evolutionary indicators we use are the standard ones: bolometric temperature T_{bol} and the ratio of submm to bolometric luminosity, $L_{\text{bol}}/L_{\text{smm}}$. T_{bol} is plotted against envelope mass M_{env} in Fig. 1. $T_{\text{bol}} = 70\text{ K}$ is used to draw a line between

Class 0 and Class I embedded protostars (Chen et al. 1995). As our T_{bol} are often upper limits where there are no near- or mid-infrared detections, we have plotted the identified protostars and the sources with upper limits separately (the SCUBA $850\mu\text{m}$ detection limits are also shown). The highest mass sources are cold Class 0 sources, which we would expect to evolve to less massive and warmer objects.

The ratio of submm to bolometric luminosity is plotted in Fig. 2. For the submm luminosity we estimate $L_{1.3}$ from the $850\mu\text{m}$ integrated flux, which is available for all our sources, measured in a bandwidth of 50 GHz and corrected to 1.3 mm using $F_{1.3} = F_{850} \times (850/1300)^{3.5}$ assuming that dust opacity is optically thin and follows a power law with index $\beta = 1.5$. The boundary between Class 0 and Class 1 sources was calculated by Andre et al. (1993) to lie at $L_{\text{bol}}/L_{1.3} = 20,000$, but in order to exclude well known Class I sources such as L1455 IRS2 we are required to lower it to $L_{\text{bol}}/L_{1.3} = 3,000$. The upper limits from IRAS introduce some uncertainty in calculating L_{bol} , and it may be that the differing analysis of the IRAS fluxes here and in Andre et al. (1993) is responsible for some the difference. However, a reduction of a factor of 4 in $L_{\text{bol}}/L_{1.3}$ for the Class 0/Class I boundary was also required by Visser et al. (2002) using a similar dataset and it seems likely that the Andre et al. (1993) limit was simply set too high on the basis of the Class I sources known at the time. The Andre et al. (1993) limit was consistent with a simple model with a single accretion rate which may not apply in all cases: the limit should increase to account for increased accretion rates at higher mass with models suggesting that the boundary lies somewhere between $L_{\text{bol}} \propto M_{\text{env}}^{1.0}$ (alternatively, $\propto L_{\text{smm}}^{1.0}$ when M_{env} is calculated with a fixed T_d as here) and $L_{\text{bol}} \propto M_{\text{env}}^{2.0} \propto L_{\text{smm}}^{2.0}$ (Smith 2000). Note that as envelope masses and submm luminosities are both proportional to the submm flux, this indicator is equivalent to plotting L_{bol} vs. M_{env} (eg. Andre & Montmerle (1994)).

A third measurement linked to the shape of the SED is the ratio of Spitzer IRAC to submm emission. This has the advantage of being reliable even when the IRAS data are confused. In Fig.2 we also plot the $3.6/850\mu\text{m}$ flux ratio vs. the $850\mu\text{m}$ flux together with rough ranges for this ratio based on the evolutionary models of Whitney et al. (2003), as a third evolutionary indicator.

Statistics (mean and standard deviation) for the three evolutionary indicators are given in Table 1. The mean value of $\log_{10} T_{\text{bol}}$ corresponds to 78 K for the total population in Perseus and 91 K for the 56 confirmed protostars (excluding the sources with upper limits on T_{bol} ; see Sect.3.1). As a temperature of 70 K is used to divide the Class 0 and Class I populations (see Sect. 3.2) these low values indicate already that the protostellar population contains a significant fraction of deeply embedded sources. The mean values of the other indicators ($\log_{10}(L_{\text{bol}}/L_{1.3})$, $\log_{10}(F_{3.6}/F_{850})$) also support this.

3.1. Protostars and starless cores

Near- or mid-infrared detections by Spitzer and/or 2MASS identify 54/103 sources ($52 \pm 7\%$) as definitely protostellar. An additional two sources are identified as protostellar on the basis of molecular outflows by our ^{12}CO outflow survey of a subset of this sample (Hatchell et al. 2006, Paper III). These sources are b1-bN/S (2) and NGC1333 SK31 (47). These were not detected by Spitzer, in the case of b1-bN/S apparently because the driving sources are still too deeply embedded, in the case of NGC1333 SK31 (46) because any associated infrared

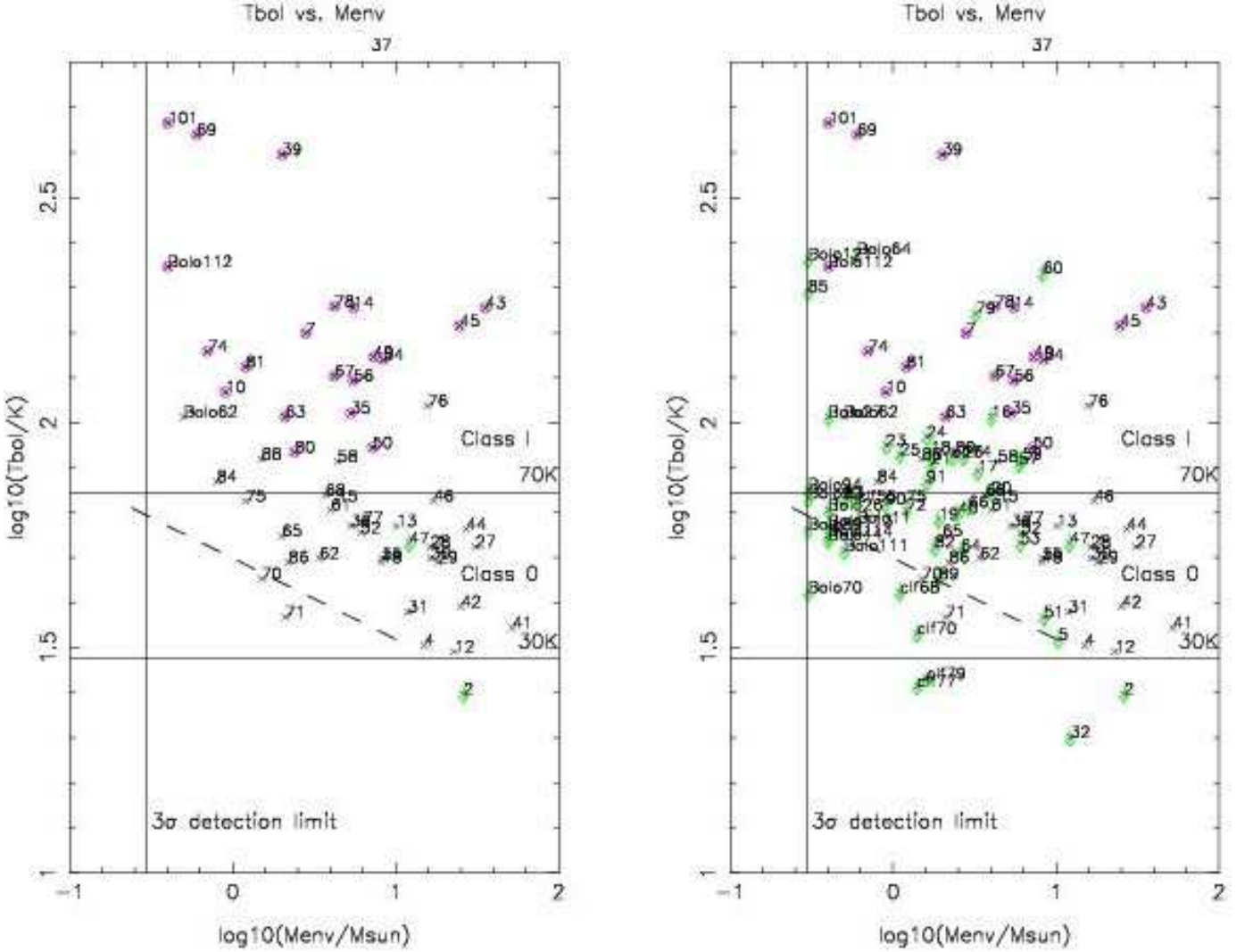


Fig. 1. Evolutionary indicators vs. envelope mass: T_{bol} vs. M_{env} . **Left:** confirmed protostars only. **Right:** all sources. Upper horizontal line: Class 0/Class I boundary at $T_{\text{bol}} = 70$ K (Chen et al. 1995). Lower horizontal line: 30 K. Solid vertical line: SCUBA detection limit. Dashed diagonal line: Early Class 0 models (Sect. 4). Class I sources (see Sect. 3.2) are marked by circles (magenta).

Table 1. Mean and standard deviation for each of the evolutionary indicators $\log_{10}(T_{\text{bol}}/K)$, $\log_{10}(L_{\text{bol}}/L_{\text{smm}})$, $\log_{10}(F_{3.6}/F_{850})$ for (top) confirmed protostars; (bottom) all sources, as plotted in Fig. 2

Confirmed protostars (56)	Mean	Standard deviation
$\log_{10}(T_{\text{bol}}/K)$	1.96 (91K)	0.33
$\log_{10}(L_{\text{bol}}/(3000 \times L_{\text{smm}}))$	-0.0256	0.617
$\log_{10}(F_{3.6}/F_{850})$	-2.92 (0.012)	1.24
All sources (103)	Mean	Standard deviation
$\log_{10}(T_{\text{bol}}/K)$	1.89 (78K)	1.04
$\log_{10}(L_{\text{bol}}/(3000 \times L_{\text{smm}}))$	-0.0431	0.691
$\log_{10}(F_{3.6}/F_{850})$	-3.28	1.07

source is masked by the scattered light from the bright neighbour NGC1333 ASR114 (45). This brings the total of confirmed protostars in Perseus up to 56. A number of sources are first identified as protostellar by this survey, namely numbers 14 and 15 (near IC348), 36 (SE of L1448), and 58, 60 and 61 (in NGC1333).

The remaining 47 sources have no positive detection of a protostellar indicator (IR, outflow) and therefore could be starless. Further infrared, radio or outflow observations are needed to detect any further protostars in this remaining sample, particularly at the low end of the mass range where any IR emission is likely to be faint and outflow masses low. Whereas the two luminosity-based indicators rely on IRAS upper limits and are not useful for the classification of the non-detections, $F_{3.6}/F_{850}$ on the other hand clearly places all sources with IR limits in either the Class 0 or starless category (Fig. 2, third panel).

Table 3.1 gives the counts of starless and protostellar cores for each subregion of Perseus. The percentage of starless cores varies between regions from 17 to 68% compared to the overall mean of 46%. To investigate whether this variation is significant, we calculate the probability of these percentages occurring by chance assuming the sources are drawn at random from a population which is 46% starless. The resulting probabilities, calculated from the binomial distribution, are given in the last column of Table 3.1. The small clusters (L1448, L1455, B1) contain small numbers each and are consistent with the cloud average. NGC1333, which has a high fraction of protostars, and IC348 and the distributed population of isolated cores, which

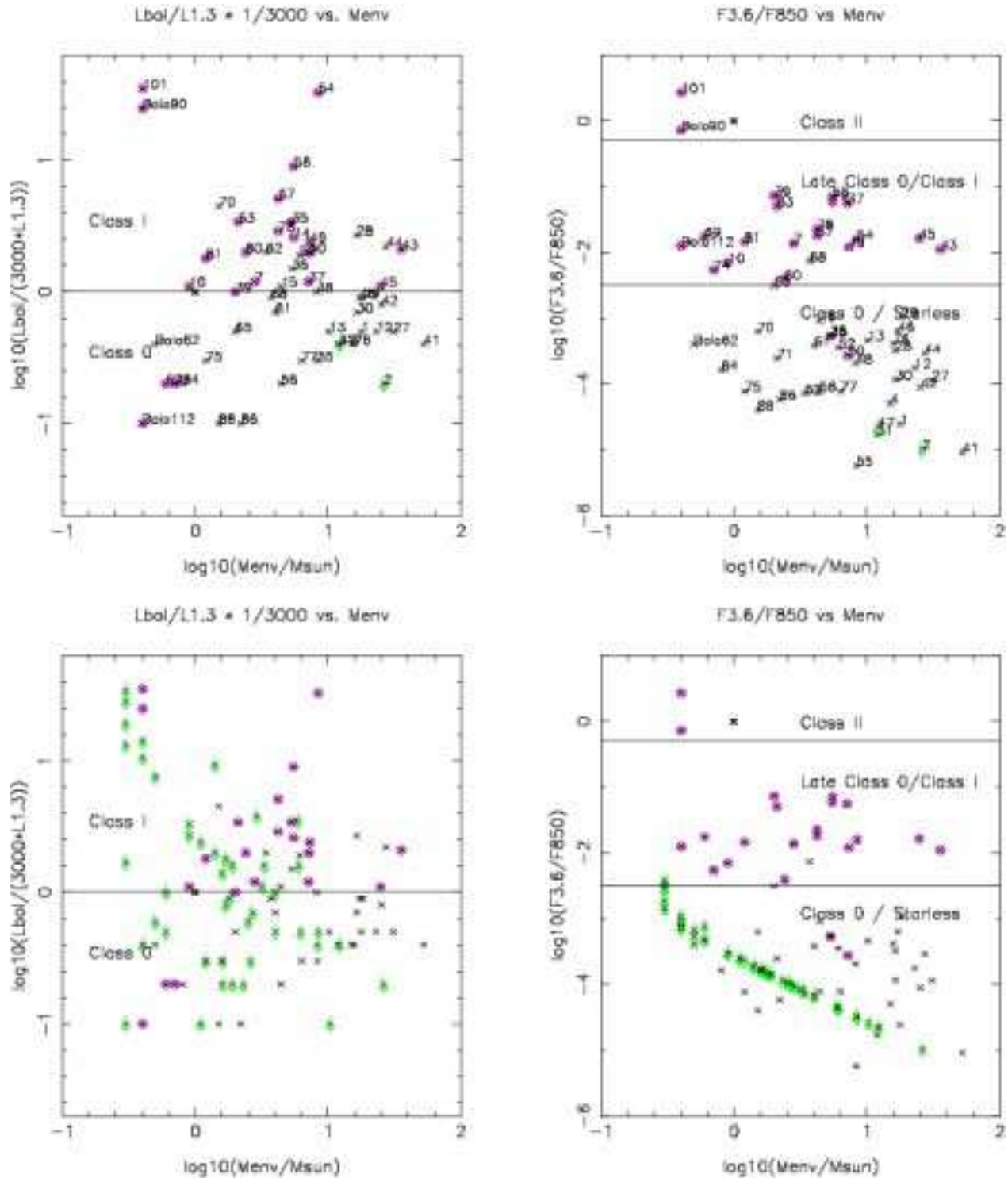


Fig. 2. Further evolutionary indicators vs. envelope mass. **Top:** confirmed protostars only. **Bottom:** all sources. **Left:** $L_{\text{bol}}/L_{\text{smm}}$, converting L_{850} to $L_{1.3}$ (Andre et al. 1993), **Right:** $F_{3.6}/F_{850}$ with classification based on the models of Whitney et al. (2003). The boundaries between classes are shown at representative values but in fact there is overlap between classes because of the effects of orientation. Class I sources (on the basis of 2/3 indicators) are marked as circles (magenta) and luminosity/flux upper limits are given for sources with no Spitzer IRAC detection.

contain larger fractions of apparently starless cores, all show significant variation from the cloud average. In each of these cases the probability of being consistent with a 46% starless fraction is less than 3%. This suggests that in individual regions, there is significant variation in the star formation rate on timescales of order the lifetime of a starless or protostellar core. Alternatively,

it is possible that the starless population in NGC1333 is underestimated as starless cores are hard to identify in richly clustered regions, and this may be biasing the cloud average to a low fraction of starless cores. Excluding NGC1333, the percentage of starless cores rises to 55% in the rest of the cloud, from which

Table 2. Counts of starless and protostellar cores by region. The last column gives the probability (from the Binomial distribution) of the counts occurring by chance assuming the sources are drawn randomly from a population with a starless fraction of 47/103.

Source	Starless	Protostellar	% starless	Prob.
NGC1333	10	26	28%	0.013
IC348 ¹	13	6	68%	0.026
L1448	1	4	20%	0.20
L1455	2	5	29%	0.21
B1	1	5	17%	0.13
Isolated	20	10	67%	0.016
Total	47	56	46%	

¹ Including the filament to the S of IC348 which contains HH211.

the IC348 and the isolated population are less significantly different.

Comparing the number of submm cores in IC348 and NGC1333 to their PMS populations of 348 and 213 stars, respectively (Sect.5), shows that IC348 is three times as rich in submm cores as NGC1333. Spitzer observations (Jørgensen et al. 2006) also show that the ratio of Class II+III to Class I sources is higher in IC348 than other parts of the cloud. The reason for this is that IC348 has been forming stars for longer (> 3 Myr, Luhman et al. 2003; Muench et al. 2003) and has had time to build up a larger fraction of Class II/III sources. IC348 has certainly been active for longer than NGC1333 and also, possibly, than the remainder of the cloud, though it is harder to be definite on this because the Spitzer observations do not rule out a more spatially extended distributed population of young PMS stars, as recently discovered in Taurus (Slesnick et al. 2006). Spitzer area selection on the basis of high A_V biases towards younger sources still associated with molecular cloud material.

We find 53% of submm cores and 57% of protostars in large clusters (IC348 and NGC1333). The fraction for protostars confirms our pre-classification result, based on the submm cores alone, of at least 40% of star formation large clusters (Paper I). These fractions are also consistent with the $> 50\%$ star formation in large clusters found by 2MASS for Perseus/Orion/Monoceros (Carpenter 2000) and $\sim 60\%$ by Spitzer for Orion/Ophiuchus (Allen et al. in prep.). Jørgensen et al. (2006) find for the youngest Spitzer-selected Class I sources in Perseus that a somewhat smaller fraction of 39% lie in clusters. The reason for the discrepancy with our results is that not all the Spitzer sources associated with submm peaks satisfy the c2d colour criteria. Jørgensen et al. (in prep.) find that positional association with MIPS sources identifies more sources in clusters as protostars than IRAC colours alone. Taken together the results are all consistent with 40% of current star formation in Perseus taking place in the distributed population of isolated stars and small (< 100 member) clusters.

From the definite detections, the ratio of protostars to starless cores is at least $47/56 = 0.8$. Previous estimates for the starless/protostellar ratio are higher, ranging from 2–3 Visser et al. (2002); Lee & Myers (1999) to 10 (Ward-Thompson et al. 1994; Jessop & Ward-Thompson 2000). This would appear to suggest that our survey is incomplete to prestellar cores, although it is difficult to believe that we underestimate the number of starless cores by the factor of 12 necessary to reach the ratio measured by Jessop & Ward-Thompson (2000).

Assuming that the star formation rate in Perseus is constant, we estimate that the average lifetime of starless cores above our

detection limit is 0.8 times the lifetime of the embedded protostars. If more protostars are later identified among the apparently starless population, the relative lifetime of detectable starless cores will be reduced. On the other hand, prestellar cores begin their life below our detection limit so the full timescale for prestellar development will be longer than the time over which we could detect them in these observations. Starless cores with a flattened central density distribution which peaks below our mass per beam sensitivity limit could still contain considerable (distributed) mass and remain undetected by our survey. We conclude that prestellar timescales are roughly equal to or longer than protostellar lifetimes.

3.2. Class 0 and Class I sources

Based on the three evolutionary indicators in Fig. 2 (T_{bol} , $L_{\text{bol}}/L_{1.3}$, $F_{3.6}/F_{850}$), 16/103 sources are certain Class I objects (see Table 4). A further six are likely Class Is based on two out of three evolutionary indicators bringing the total number of Class Is to 22. More spectral/spatial information is required in order to determine the true nature of a further five sources (58,76,84,88, and Bolo62), which are classified Class I on T_{bol} but are classified as Class 0 on the other two indicators. For these sources, the temperature is high but the estimated luminosity is too low to be consistent with a Class I identification. We assume these are Class 0. The classifications based on each evolutionary indicator, and the majority vote, are given in Table 4 and the spatial distribution of the sources is shown in Fig. 6.

Thus, of the 56 confirmed SCUBA-detected protostars, the number of Class Is is only 22 out of 56 (39%). The remaining 34 confirmed protostars must be Class 0. On the basis of these counts, SCUBA-detected Class 0s are more common than Class Is in Perseus.

That raises the question of how many Class I sources we fail to detect with SCUBA because they fall below our detection limit. We can only detect 10 K envelope masses of $0.3 M_{\odot}$, and are complete above $0.5 M_{\odot}$. Class I sources begin by definition with an envelope mass equal to the stellar mass and the envelope mass subsequently reduces. For Class Is forming stars below about $0.6 M_{\odot}$, therefore, we would not expect to detect the envelope for more than half of the Class I lifetime.

We can, however, estimate the number of Class Is which we fail to detect with SCUBA as Spitzer is more sensitive to Class I sources. Jørgensen et al. (2006) make an independent estimate of the number of Class I sources in Perseus from the Spitzer survey, which covers a similar area as SCUBA, on the basis of their infrared spectral index in the Spitzer IRAC and 2MASS bands. As the infrared spectral index classification (Greene et al. 1994) does not include a separate category for Class 0 sources (as at that time they were not detected in the infrared) both Class 0 and Class I sources are included in the Jørgensen et al. (2006) Class I count of 54. Of their sources, 14 lie outside the SCUBA map boundary and 29 coincide with SCUBA-detected protostars. The remaining 11 sources in the Jørgensen et al. (2006) Class I list lie within the SCUBA map but were not detected in the submillimetre. These could be Class I sources with low envelope masses below the SCUBA detection limit. Including these Spitzer detections, the total number of Class I sources in our mapped area could therefore be as high as $22 + 11 = 33$, bringing the total number of protostars in Perseus up to $56 + 11 = 67$. The 34 confirmed Class 0 sources therefore still make up more than half of the total number of protostars. This fraction may be even higher if more of the IR non-detections later turn out to be protostellar through identification of molecular outflows or radio sources, as

these must also be Class 0: the limits on the infrared emission rules out Class Is on the basis of $F_{3.6}/F_{850}$ (Fig. 2).

The ratio of Class 0s to Class Is in Perseus is quite unlike Ophiuchus and Taurus clouds where Class I sources outnumber Class 0s by 10:1 (Andre & Montmerle 1994; Motte & André 2001) and exceeds even Serpens where at least 25% of sources are Class 0 (5 Class 0s identified by Hurt & Barsony (1996) compared to 19 Class Is from Kaas et al. (2004)). Although it is possible that there are some further undetected Class I sources which were not identified by Jørgensen et al. (2006) it is hard to imagine (given the sensitivity of the Spitzer c2d survey) that these outnumber the detections by 10:1.

One explanation for the large numbers of Class 0 sources in Perseus could be that Perseus has undergone a recent burst of star formation – perhaps triggered by 40 Persei, a B0.5 star in Per OB2 (Walawender et al. 2005; Kirk et al. 2006) – and this has produced a large number of protostars which are still in the Class 0 phase. Perseus has been forming stars from at least 3–4 Myr ago IC348 until the present day (Luhman et al. 2003; Muench et al. 2003). Therefore multiple triggering events would be required to explain both the earlier formation of IC 348 and the star formation in the last few $\times 0.1$ Myr, which would be necessary to explain a current population of Class 0s. The average star formation rate in Perseus is consistent with steady star formation and a protostellar core lifetime of a few $\times 10^5$ years, in agreement with previous studies (see Sect. 5, Paper I).

An obvious difference between Ophiuchus and Taurus on the one hand and Perseus, Serpens and Orion on the other is that the protostellar envelopes are more massive in Serpens, Perseus and Orion. Roughly similar flux sensitivity limits mean observations trace the higher-mass end of the population in these more distant clouds (Perseus 320 pc, Serpens 259 pc, Orion 400 pc compared to Ophiuchus and Taurus, both at ~ 150 pc). The Class 0 sources in Serpens have envelope masses above $0.6 M_{\odot}$ (Hurt & Barsony 1996); the Perseus Class 0s all have masses above $0.5 M_{\odot}$ (see Fig. 3). In fact, no Class 0 sources with envelope masses less than $\sim 0.2 M_{\odot}$ are found in any of these clouds, or indeed in the recent compilation of known Class 0 sources (Froebrich 2005). This is very clearly seen in Fig. 2 of Bontemps et al. (1996), and is partly due selection effects: targetted submm surveys were largely based on known infrared and radio sources and therefore only picked up Class Is and a limited number of high mass (luminous) Class 0s. Our SCUBA survey, on the other hand, is more sensitive to Class 0s than starless cores or Class I sources, though we may be missing the equivalents of many of the lower-mass objects in Rho Oph and Taurus in Perseus. Note that the majority of Perseus Class 0 sources would still have masses above $0.2 M_{\odot}$ even if the masses were reduced by the maximum uncertainty factor of 10.

The higher mass of the Perseus population could be directly responsible for longer Class 0 lifetimes, if the evolution of protostars depends on mass in a way which favours long Class 0 lifetimes for higher mass objects. Such a variation is predicted, for example, by gravoturbulent fragmentation (Schmeja & Klessen 2004). It is also a consequence of the competitive accretion model (Bonnell et al. 2001; Bate et al. 2003; Bonnell & Bate 2006), as higher mass cores continue to acquire material from the surrounding cloud during the Class 0 phase and only embark on the Class I loss of envelope mass when the reservoir of material has run out.

The Class I/Class 0 classification of protostars is also affected by mass, because in practice the classification relies on observational indicators such as T_{bol} rather than a direct comparison of the mass in the envelope and the stellar mass, which

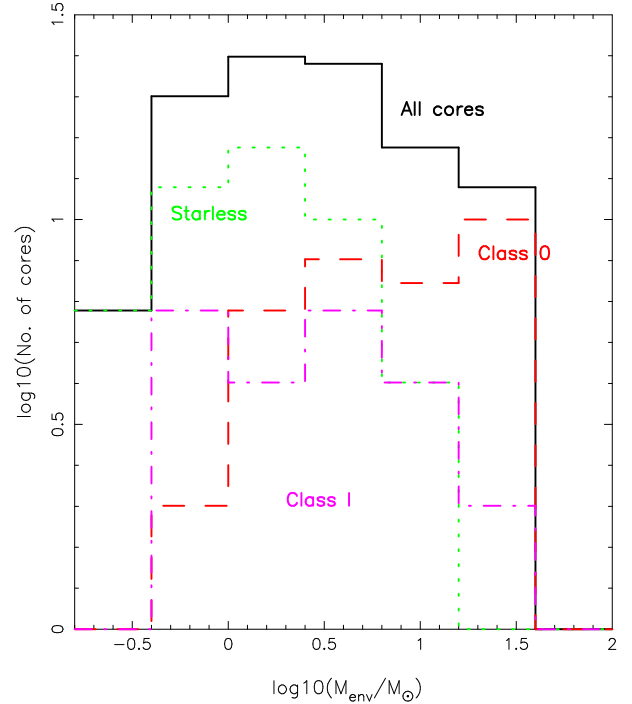


Fig. 3. Histogram of masses for all sources (solid line), Class Is (dot-dash), Class 0s (dashed) and starless cores (dotted line).

cannot be directly measured. More massive sources also have greater optical depth in their envelopes and therefore SEDs which peak at longer wavelengths for the same dust geometry. As a source evolves, loses envelope mass and evacuates a cavity, it emits more infrared radiation relative to submillimetre, and passes from Class 0 to Class I on the basis of $L_{\text{submm}}/L_{\text{bol}}$ or T_{bol} . More massive sources, with greater initial optical depth, have to lose relatively more of their envelope mass to reach the required T_{bol} threshold to be classified as Class I. The lower envelope mass sources have higher T_{bol} and $L_{\text{submm}}/L_{\text{bol}}$ because of lower envelope optical depth and apparently make the transition from Class 0 to Class I earlier in their evolution. Fig. 3, which shows the mass distribution for the cores separated by class, shows that the Class 0 sources tend to have higher masses than the Class Is. In order to investigate this effect further, we model the emission from a Class 0 geometry envelope with a range of masses in Sect. 4 and discuss the implications for the classification of Class I and Class 0 sources, but before we can do this we consider the relationship between mass and luminosity.

3.3. Relationship between L_{bol} and M_{env} .

The relationship between luminosity and envelope mass is shown in Fig. 4. Mass is measured from the submm flux assuming a constant temperature of 10 K whereas luminosity is measured by integration across the entire spectrum and thus is most dependent on the IRAS fluxes. Note that although a higher luminosity source will have higher temperature components than a lower luminosity source of equivalent mass, the bulk of the mass is in cold gas therefore the constant temperature assumption in the mass calculation still holds. There is a general trend for higher mass sources to have higher luminosity. But there is not a tight relationship between envelope mass and luminosity. This scatter is intrinsic, and due to the fact that we are plotting not just Class I protostars (as Reipurth et al. (1993)) but

also Class 0s, which have higher masses for the same luminosity. This scatter was also seen in the sample of Bontemps et al. (1996), and it is this scatter which enabled us to use $L_{\text{bol}}/L_{\text{smm}}$ which is proportional to $L_{\text{bol}}/M_{\text{env}}$ to estimate the evolutionary state of a core (Sect. 3).

Higher mass accretion rates – and therefore higher luminosities – are clearly driven by higher initial envelope masses. The evolution of luminosity with mass depends on the details of the accretion process, and evolutionary tracks for $L_{\text{bol}}-M_{\text{env}}$ have been suggested based on various accretion models (see Froebrich 2005, and references therein). A possible scenario is that mass accretion rates and therefore accretion luminosity initially increase exponentially and then reduce, resulting in $M_{\text{env}}-L_{\text{bol}}$ tracks which rise rapidly in luminosity (up and slightly to the left in Fig. 4) during the Class 0 stage and then decrease in both luminosity and mass (down and to the left in Fig. 4). An example of such an evolutionary track, from Smith (2000, Fig. 6), scaled by a factor 30 in mass in order to match the high envelope masses in Perseus, is plotted in Fig. 4. In this example the luminosity decrease during the Class I phase follows $L_{\text{bol}} \propto M_{\text{env}}^\alpha$ with power law index α between 1 and 2. Of course, accretion rates and luminosity may also vary during both the Class 0 and Class I evolutionary stages if accretion is variable, as is known to be the case for mass ejection in the jet (eg. Hartigan et al. 2005)), so evolutionary tracks are probably not as simple as this model represents.

Luminosity evolution during the Class 0 stage can produce a selection bias towards high mass Class 0s as they reach luminosities at which infrared or outflow emission can be detected earlier in their lifetimes. Therefore, higher mass Class 0s may be visible as protostars for longer. This bias is strong if the luminosity evolution is slow and weak if it is fast. If mass accretion rates rise very rapidly to a maximum during the Class 0 phase (Henriksen et al. 1997; Schmeja & Klessen 2004; Whitworth & Ward-Thompson 2001; Stamatellos et al. 2005), then the Class 0s will spend most of their lifetime close to the Class I boundary and the number of Class 0s which remain undetected will be small. There is supporting evidence for this fast luminosity evolution in Fig. 4 as high mass sources with low luminosities are absent. This suggests either that the time taken to reach high luminosities (roughly, within two orders of magnitude of the maximum for a given mass) is much shorter than the subsequent evolution through the Class 0 and Class I phases, or the proposed evolutionary track is wrong. For example, high mass Class 0 sources could evolve from lower-mass Class 0 sources through competitive accretion.

We fitted a straight line to $\log_{10}(L_{\text{bol}})$ vs. $\log_{10}(M_{\text{env}})$, assuming uncertainties in $\log_{10}(M_{\text{env}})$ of 0.5 (factor of 3) and $\log_{10}(L_{\text{bol}})$ of 0.3 (factor of 2). For the entire sample of known protostars,

$$\log_{10}(L_{\text{bol}}) = \log_{10}(M_{\text{env}}) \times (1.96 \pm 0.36) - (1.09 \pm 0.30).$$

Fitting just Class 0 sources, the gradient is similar but the luminosities are lower:

$$\log_{10}(L_{\text{bol}}) = \log_{10}(M_{\text{env}}) \times (1.88 \pm 0.46) - (1.43 \pm 0.46).$$

Fitting only Class Is, the fit is

$$\log_{10}(L_{\text{bol}}) = \log_{10}(M_{\text{env}}) \times (1.85 \pm 0.52) - (0.46 \pm 0.35),$$

with a gradient consistent with the index of 1.6 found for Class I sources driving Herbig-Haro objects (Reipurth et al. 1993). These fits are plotted in Fig. 4. There are two selection effects: firstly, low-luminosity low-mass Class 0s are selected

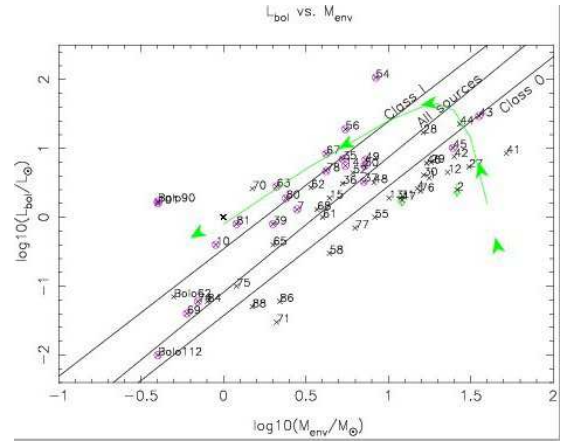


Fig. 4. Bolometric luminosity vs. envelope mass for confirmed protostars. Class I sources (see Sect. 3) are marked with circles. Power law fits to all sources, Class 0s and Class Is are shown (see text). An evolutionary track from Smith (2000), scaled by a factor 30 in mass, is shown for illustration with arrows at $\log_{10}(\text{age}) = 3.5, 4.0, 4.5, 5.0, 5.5$ yr (in green)

against so the slope of the best fit line for Class 0s and the whole sample are probably too low; secondly, we believe some of the low mass Class I sources should be reclassified as Class 0s (see Sect. 4), so the slope of the best fit line for Class Is is probably too high. The uncertainties on the fits are high and the scatter is large, so they should in any case be treated with caution. Nonetheless, the results are consistent with Class Is having generally higher luminosities than Class 0s and a power law index between 1 and 2, consistent with the Smith (2000) model.

4. Radiative transfer modelling of Class 0 geometry sources with different masses

We computed radiative-transfer models of Class 0 objects using the Monte-Carlo radiative-transfer code `TORUS` (Harries 2000; Harries et al. 2004). The code is based on the radiative-equilibrium method described by Lucy (1999) and uses an adaptive mesh in order to adequately resolve sub-solar-radius scales in parsec-scale computational domains (Kurosawa et al. 2004).

Our Class 0 geometry is based on the models described by Whitney et al. (2003). In brief, this consists of a blackbody source of radiation surrounded by a flared accretion disc which is in turn embedded in an infalling envelope. Low-density bipolar cavities exist perpendicular to the disc. For simplicity we adopt ISM-type grains, although more sophisticated models could allow for evolution of both the grain size distribution and the dust chemistry. We give full details of the density description, along with the dust grain size distribution and chemistry adopted, in the Appendix.

4.1. Model parameters

We computed models for a range of envelope masses between $0.05 M_{\odot}$ and $10 M_{\odot}$. The luminosity for each model was selected by adjusting R_* to follow $\log_{10}(L_{\text{bol}}) \propto 1.5 * \log_{10}(M_{\text{env}})$ with luminosities appropriate to masses calculated at 30 K (consistent with Bontemps et al. (1996)). The resulting absolute luminosities are higher (for the same mass) than for the Class 0 sources (Sect. 3.3) but the relative scaling (and therefore the relative effect on T_{bol}) is consistent. A constant $M_{\text{env}}:M_*$ ratio of 3

M_{env}/M_{\odot}	0.05	0.1	0.2	0.5	1.0	3.0	10.0
T_{bol}/K	67.4	68.1	68.1	54.8	48.1	40.1	34.9

Table 3. Dependence of T_{bol} with M_{env} for Class 0 models with identical geometry.

(Whitney et al. 2003) was assumed to represent the same evolutionary stage for sources of different masses. The basic model parameters are listed in Table A.1.

We computed all the SEDs assuming an inclination of 90° ; the shape of the SED is essentially independent of viewing angle except for pole-on orientations, in which case the near-to-mid IR portion of the spectrum is enhanced by direct and scattered radiation that escapes along the polar cavities.

4.2. Model results

The dependence of T_{bol} with M_{env} for Class 0 models with identical geometry is given in Table 4.2.

This dependence is plotted as a dashed line in Fig.1. Low mass Class 0 sources have significantly higher T_{bol} than their higher-mass counterparts, for the same geometry. Our models of young Class 0 sources reach $T_{\text{bol}} \sim 70$ for $0.2 M_{\odot}$ and below and are on the borderline of being classified as Class I. Furthermore, although we chose to model a geometry representative of the very earliest Class 0 sources, a $T_{\text{bol}}-M_{\text{env}}$ dependence also holds for other geometries as it is a fundamental property of radiative transfer, so models of more evolved envelopes with a higher luminosity to mass ratio and a wider outflow cavity would cross the Class 0/Class I boundary at $T_{\text{bol}} = 70$ K at higher M_{env} . Low mass sources are therefore more likely to be classified as Class I on the basis of T_{bol} despite having a Class 0 type envelope geometry.

4.3. Class 0 and Class Is revisited.

Using the models, we can revisit the classification of protostars in Perseus and consider why we see so many more Class 0 sources compared to lower-mass samples such as Bontemps et al. (1996). All the Class 0 sources which have T_{bol} above the predictions of the model as shown in Fig.1 would be reclassified as Class I sources on the basis of T_{bol} if their envelopes were reduced to $< 0.2 M_{\odot}$ while retaining the Class 0 geometry. This means that essentially all our Class 0 sources – excluding only the three sources b1-bN/S (2), NGC1333 SK22(70) and HH340B(71) – would have been classified as Class I had they had the same geometry but lower mass. This conclusion holds even if we were to calculate envelope masses assuming a constant 30 K rather than 10 K, which reduces the masses by a factor of 7, for consistency with Bontemps et al. (1996): in that case 7 rather than 3 sources would retain their Class 0 classification.

Thus, if Perseus had been forming lower mass stars with envelope masses under $0.2 M_{\odot}$, but with the same envelope geometry, the fraction of sources classified Class 0 to Class 1 would drop to around 7/49, similar to the 20% found by Bontemps et al. (1996). This potential misclassification of Class 0-geometry sources with low envelope masses could account entirely for the high number of sources classified Class 0 in Perseus – which we believe are truly Class 0 sources (see below) – compared to studies of lower mass regions where we believe many Class I-classified sources may in fact have Class 0 geometry.

If this is the case, and Perseus is representative, then the relative lifetimes of Class I and Class 0 phases are not, as earlier suggested, 10:1 (Andre & Montmerle 1994; Motte et al. 1998), but instead roughly 1:1, as found in Perseus and in Lynds dark clouds (Visser et al. 2002), assuming that the star formation rate is constant.

How are the other SED-based evolutionary indicators shown in Fig.2 affected by mass? The SED-based indicator $F_{3.6}/F_{850}$ should also decrease towards higher masses for the same envelope geometry as the peak of the SED shifts longwards (see Fig. A.2). The remaining evolutionary indicator, $L_{\text{bol}}/L_{\text{smm}}$, is based on input properties of the models as M_{env} is derived from L_{smm} . From Fig. 4, and as also suggested by models (Smith 2000), the $L_{\text{bol}}/M_{\text{env}}$ boundary between Class I and Class 0 sources should rise with M_{env} and therefore so should $L_{\text{bol}}/L_{\text{smm}}$. On this indicator, low mass sources should require lower $L_{\text{bol}}/L_{\text{smm}}$ ($L_{\text{bol}}/M_{\text{env}}$) to be classified as Class 0. The higher masses in our sample do not explain why we have to set a low $L_{\text{bol}}/L_{1.3}$ boundary at 3000 rather than 20,000 (Andre et al. 1993), as we would expect $L_{\text{bol}}/L_{\text{smm}}$ at the Class 0/Class I boundary to rise with mass leading to a higher threshold for Perseus.

Could many of the apparent Class 0 sources in Perseus be misclassified and in fact be Class Is? As higher-mass sources have lower T_{bol} for the same geometry, it is the warm, high-mass sources in the Class 0 classification which might in fact be Class Is despite T_{bol} less than 70 K. This assumes that the Class 0/Class I boundary lies roughly parallel to the $M_{\text{env}}-T_{\text{bol}}$ track shown on Fig.1, only higher in T_{bol} . Therefore sources such as L1448 NW (27), NGC1333 IRAS2 (44), and NGC1333 IRAS7 (46), HH 211 (12), L1448 NW (27) and L1448 C (29) are the most likely sources to have a Class I-like geometry. In the case of some these sources their high T_{bol} can be explained by their multiplicity (see Sect.5.2). However, this list contains many classic bright Class 0 sources, which cluster in this part of the $M_{\text{env}}-T_{\text{bol}}$ diagram; if the number of Class 0s in Perseus is to be reduced by reclassification then Class 0 prototypes such as HH211 and L1448 C will be among the first sources to go. This seems unlikely as the collimated molecular outflows from these sources also support the young age estimates (eg. Hirano et al. 2006; Dutrey et al. 1997). Therefore we conclude that it is unlikely that a large number of our Class 0 sources need reclassification on the basis of the mass dependence of the evolutionary indicators. It is more likely that we, too, have misclassified low-mass sources with T_{bol} close to 70 K as Class I when they should be Class 0 – eg. sources 84 and Bolo62 which fail on two evolutionary indicators.

It is clear the evolutionary indicators – T_{bol} , $L_{\text{bol}}/L_{\text{smm}}$ $F_{3.6}/F_{850}$ – which we use to classify protostars should all vary with mass. All of these evolutionary indicators are currently set, based on models or observations, at a fixed boundary appropriate to only a small range of masses. How exactly they vary at the Class 0/Class I boundary needs further investigation. It is clear that more radiative transfer modelling is needed in order to define the observable characteristics of the Class 0/Class 1 boundary at $M_{\text{env}} = M_*$ and before the numbers of sources in each class can be determined reliably. Alternatively, it may make sense to consider all the embedded sources (Class 0 and I) as a single class with variation within that class.

4.4. Protostellar brown dwarf candidates

Our modelled Class 0 geometry, with only a narrow outflow cavity, is intended to correspond to the earliest stage in protostellar

evolution. If this were true then these models would define a “birthline” for protostars with no protostars falling below the line. Fig.1 shows that the majority of protostars do indeed lie above the line. Protostars must begin with lower luminosities than those we have modelled, but the early phase is both short-lived and difficult to detect in the infrared or outflows. Protostars then are predicted to evolve steeply upwards and to the left in the $M_{\text{env}}-T_{\text{bol}}$ diagram (Smith 2000; Froebrich 2005, eg.).

Protostellar brown dwarfs forming in isolation, if such things exist, will be found among the sources with envelope masses up to a few times the substellar mass limit and fitting the Class 0 envelope model. Our lowest mass, lowest T_{bol} candidate Class 0 brown dwarfs with Spitzer detections are sources 84 ($0.77 M_{\odot}$, 74 K) and Bolo62 ($0.5 M_{\odot}$, 103 K), both of which are too massive and warm to be serious Class 0 brown dwarf candidates. Earlier, more embedded candidates may be found among the low mass sources without Spitzer detections, if any of these can be confirmed as protostellar. These sources include the Bolocam sources which were only detected by SCUBA at the 3σ level and cluster around the 3σ detection limit in Fig.1, of which the lowest T_{bol} candidate is Bolo70, if this source can be demonstrated to be protostellar. Given the dependence of T_{bol} on M_{env} and that in protostars the main source of luminosity is accretion, young brown dwarfs are likely to rapidly evolve to $T_{\text{bol}} > 70$ even in the Class 0 phase.

5. Lifetime of the protostellar phase

To estimate the full duration of the protostellar phase, Class 0 plus Class I, we can compare our census of protostars in Perseus to the older pre-main-sequence (PMS) T Tauri population, for which age estimates exist, following the method of Kenyon et al. (1990) and Wilking et al. (1989). Most of the Class II and III sources near the Perseus molecular clouds lie in the two main clusters IC348 and NGC1333. On larger scales, the OB association Per OB2 contains 90% of the B stars in Perseus but with photometric age estimates of 6–15 Myr (de Zeeuw & Brand 1985; Gimenez & Clausen 1994) we assume that IC348 and NGC1333 contain the only star formation in the last 5 Myr. Using the pre-main-sequence population and age estimates for these two clusters, we can estimate the recent star formation rate and compare to the currently forming population of embedded protostars.

The most complete estimate of the population of IC348 is 348 ± 47 stars with $m_K \leq 16.75$ in an area of 20.5×20.5 arcmin² (Muench et al. 2003). The mean age for this cluster is 3–4 Myr (Luhman et al. 2003; Muench et al. 2003, Mayne, priv.comm.). Any star formation before this time was either at a lower level or is an artefact due to the uncertainties in ages derived from colour-magnitude diagrams (Hartmann 2001; Burningham et al. 2005).

Wilking et al. (2004) detected a total of 213 stars in NGC1333 above a similar magnitude limit of $m_K = 16$ (note the K-band luminosity function is falling off rapidly at these magnitudes, so the slight difference in sensitivity between the two PMS surveys makes little difference to the counts). In the centre of the northern cluster alone, they detect 126 stars of which an estimated 15 are field stars. Assuming the field star fraction is the same in the wider area, the total of pre-main-sequence stars is 188 ± 25 stars. Age estimates for individual stars in NGC1333 vary from 0.3 Myr (Wilking et al. 2004) to several Myr (Aspin 2003), though it is generally accepted to be less than 1 Myr old.

The total number of PMS stars in both clusters is therefore 536 ± 53 stars. As both Wilking et al. (2004) and Muench et al.

(2003) find that the IMF is falling off towards lower masses, better sensitivity to PMS stars within the observed cluster regions would not increase this number significantly; this is an almost complete census of the PMS population within these limited areas. SCUBA, Spitzer and 2MASS observations all have found that the fraction of stars forming in the distributed population in Perseus, in isolated cores or small groups outside the main IC348 and NGC1333 clusters, comprises 20–40% of the total (ie. an additional 20–60% over NGC1333 and IC348) (Carpenter 2000; Hatchell et al. 2005; Jørgensen et al. 2006; Megeath & al. 2006; Allen et al. in prep.). To get the total past star formation rate in Perseus we correct the star counts in the clusters by this factor, including the $\sim 20\%$ uncertainties. An additional population of 20–60% increases the star count over the past 3.5 Myr to 750 ± 130 stars.

We compare the PMS count to the population of 56 protostars identified in the submm (Sect. 3.2).

In order to estimate a lifetime for the protostellar population we have to make an assumption about the current star formation rate. The simplest assumption is that the star formation has been constant over the lifetime of star formation in the region. There does not appear to be any strong evidence, from the Spitzer data or otherwise, that this is either a particularly active or inactive time for star formation in Perseus, which would justify using a different value than the time average for the current star formation rate. Star formation in individual regions of the cloud does vary with time – for example, star formation in NGC1333 only began ~ 1 Myr ago. However, the temporal variations in the star formation rate in individual regions are assumed to average out when spatially averaged over the whole cloud. Clearly, the more regions one includes in such a calculation, the more likely this assumption is to hold, and in a single molecular cloud with just two main clusters and a distributed population, temporal variations in the star formation rate are likely to be our greatest source of error.

The average star formation rate derived from 750 ± 130 PMS stars formed over the last 3.5 Myr is 214 stars per Myr with 95% confidence limits of 168–306 stars per Myr, where the uncertainties include only the uncertainties on the PMS count and age.

A lower limit of 0.26 Myr on the protostellar lifetime is calculated by assuming the 56 confirmed submm-detected protostars are the entire protostellar population. However, this simple estimate does not take into account any corrections for either completeness and multiplicity, both of which may increase the true number of protostars above those detected.

5.1. Completeness

If we are going to compare source counts at the protostellar and PMS stages, we need to ensure that we are comparing like with like and selecting objects corresponding to a similar range of final stellar masses at each stage. The PMS studies extend well below the brown dwarf limit. Our SCUBA survey, on the other hand, is incomplete to low mass protostars: the 3σ detection limit for 10 K protostars is $0.3 M_{\odot}$. Spitzer c2d has a similar sensitivity limit to embedded sources (Evans et al. 2003), though a complementary bias towards the more evolved cores, resulting in a small number of additional MIR detections of protostars. It is unlikely that either of these surveys would have detected the protostellar phase of any lower-mass PMS objects if they form individually. Stars of $\sim < 0.1 M_{\odot}$ may never have had envelope masses above the detection limit of $0.3 M_{\odot}$ and simply would not be detected by our SCUBA survey. As envelope mass reduces with time until it reaches zero, essentially any protostar

ultimately drops below the submm detection limit. What fraction of the total number of protostars do we detect? The variation of protostellar envelope mass with time is poorly understood, and made more complex by disparate estimates for the relative numbers of Class 0 and Class I sources, so using models of envelope evolution does not seem to be a reliable basis for an estimate. The detection limits are also made more complex by the presence of protostellar disks, which can also be detected in the submm. Uncertainties in the envelope masses due to uncertain dust opacities, dust temperature and cloud distance introduce further systematic errors when comparing the two populations. In summary, we must take into account a fraction of undetected protostars, but exactly how large that fraction is is hard to estimate.

5.2. Multiplicity

We also have to correct for multiplicity. If a significant fraction of protostellar cores form multiple sources simultaneously, and those sources could be resolved in the infrared studies once they reached the PMS stage (ie. are not close binaries), then the number of protostars is higher than the number of protostellar cores which we count and we will underestimate the protostellar lifetime. Note that if cores form stars sequentially and then eject them then the number of cores will still represent the number of stars being formed at any one time, so sequential star formation does not introduce any error in our lifetime estimate.

How much evidence is there for multiplicity in our sample? Some of the cores in our sample are known to be forming binaries or higher-order systems: could these result in multiple infrared detections? NGC1333 IRAS4A and B are each binaries or higher order systems (Lay et al. 1995); NGC1333 SVS13 is a binary (Anglada et al. 2000); L1448 IRS2 is a binary (Wolf-Chase et al. 2000; O’Linger et al. 2006). Most of these would not be resolved at the T Tauri stage in infrared studies equivalent to those of IC348 or NGC1333. The overall binary fraction in IC348 is $19 \pm 5\%$ (Duchêne et al. 1999) and we estimate the fraction of resolved binaries to be $< 20\%$ of this, assuming the period distribution in Duquennoy & Mayor (1991). On that basis $4\% \pm 1\%$ of our sources will form binaries which would be resolved in the infrared at a later stage, which introduces only a small correction to the lifetime.

Do we see any evidence for protostar-protostar multiplicity other than close systems which would not be resolved in the PMS studies? With a $14''$ beam we might expect to find confusion especially in the clustered regions, and we do. L1448 N A/B (27) is an obvious example. B1-BN/S (2) is potentially a pair of protostars, though there is no clear detection of a second infrared source or outflow (Hirano et al. 1999a). Several NGC1333 sources are also multiple when examined at higher resolution (Sandell & Knee 2001) or with radio observations Rodriguez et al. (1997); Rodríguez & Reipurth (1998): IRAS2A/B (44), SSV13 (43), IRAS7 (46), and ASR114 (45) are all believed to contain multiple protostars with separations that would be resolved in the infrared. These sources are among the most massive in our sample and therefore the easiest in which to detect multiplicity. On the above count of six sources we estimate 10% is a lower limit to the number of cores containing multiple protostars, but the true number is likely to be more as only these massive, luminous protostars have been investigated with sufficient sensitivity and resolution. Note that this multiplicity is not easily identified in the infrared: many of these sources contain a luminous protostar which swamps fainter neighbours and in the few cases where one can resolve multiple Spitzer detec-

tions, these appear to be due to shocked H_2 outflow components rather than additional protostars.

It is also possible that some of our cores contain both a protostar and a collapsing prestellar core. Such sources would appear overmassive for their luminosity and therefore classified Class 0. Class 0 sources account for slightly more than half our total population of cores, which places an upper limit on the number of cores of this type.

Increasing multiplicity also increases the protostellar lifetime, as our submm core count again underestimates the true number of protostars. This effect is not entirely independent to that of incompleteness, however, as many of the objects formed in multiple cores will be low mass sources which would not have been detected as protostars if isolated because of their low envelope masses.

5.3. Bayesian probability-based estimate of protostellar lifetimes.

Our current state of knowledge does not allow us to place definite numbers on either the mean fraction of the protostellar lifetime to which our SCUBA survey is sensitive or the multiplicity of the submm sources. But it does allow us to place some limits and also make some informed estimates about the most likely scenarios.

We can use this additional information to improve on the simple lower limit on the lifetime calculate earlier and estimate the range of possible protostellar lifetimes. To do this we use a Bayesian methodology to derive a probability distribution for the protostellar lifetime, based on probability distributions for the factors involved – the number of protostars, number of pre-main-sequence stars, and duration of star formation in IC348. The Bayesian treatment has the advantage of allowing arbitrary distributions to be treated rather than making the usual implicit assumption that all variables follow a normal distribution. In our case our state of knowledge about the number of protostars, which has a well-defined lower limit but a long tail to high numbers (allowing for high multiplicity or incompleteness), are poorly represented by a Gaussian, and therefore a more complex treatment is required. The other parameters - the age of IC348 and the number of PMS stars - are represented by Gaussian variables in the usual way.

Considering in detail the probability distribution for the number of protostars, $P(N_{\text{proto}})$, we have a lower limit: we know that there are at least 56 protostellar cores. Including the additional Spitzer detections, we take a count of 67 protostars to be more probable than 56. Taking into account the known multiplicity of at least 10%, we would anticipate that 74 protostars is even more probable. We represent this by a rising probability from 56 to 74 following a partial Gaussian $\exp -(N_{\text{proto}} - 74)^2 / (2 \times 9^2)$. Above this count we have to correct for the unknown number of undetected low-mass envelopes and the amount of multiplicity, about which our state of knowledge is very uncertain, but again we can place some limits. If protostellar envelope masses mirror the IMF, then we would expect our SCUBA detections above $0.3M_{\odot}$ to account for only 40% of the total population (Muench et al. 2003) and the total count could number as many as 140; however, as envelopes have, on average, masses greater than the resulting protostars and some lower-mass stars will form inside higher-mass multiple cores we consider such a high count to be unlikely. To represent this, we assign a probability above the peak probability at $N_{\text{proto}} = 74$ initially remaining high but ultimately falling steeply to a low but finite probability to values close to the maximum of 140, following an exponential

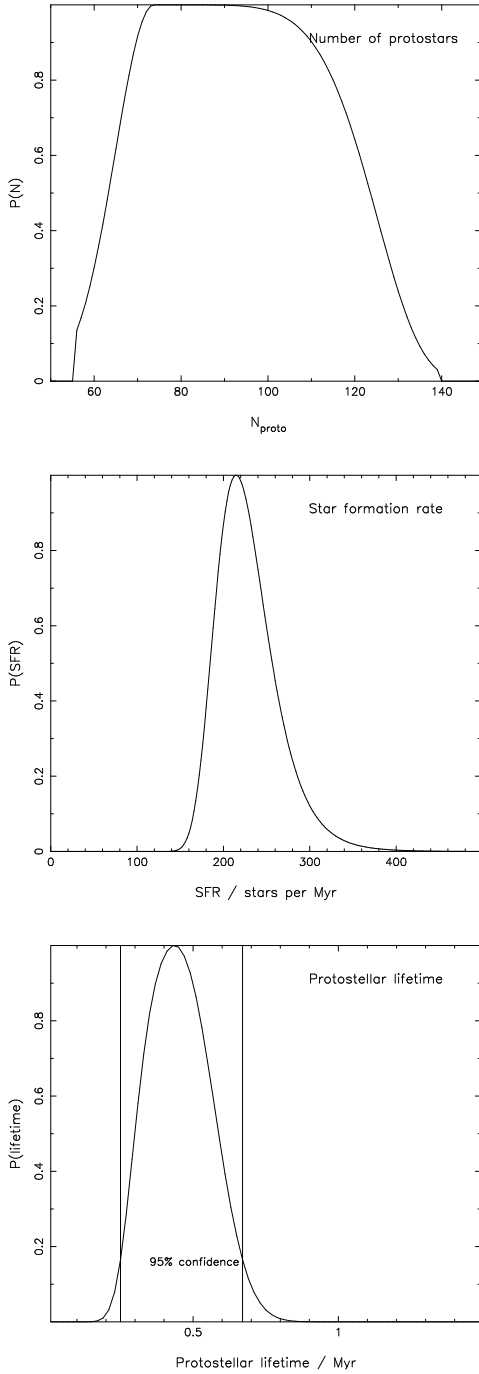


Fig. 5. Probability distribution for protostellar lifetimes. **Top:** Assumed probability distribution for the number of protostars based on SCUBA detection of 56 above $0.3M_{\odot}$. **Centre:** Probability distribution for the star formation rate (SFR) based on the duration of star formation in IC348 and the number of pre-main-sequence stars in Perseus. **Bottom:** Resulting probability distribution for the protostellar lifetime.

$P(N_{\text{proto}}) \propto \exp(-(N_{\text{proto}} - 74)/54.8)^6$. The resulting composite probability distribution is shown in the top panel of Fig. 5. These assignments of probabilities are necessarily somewhat arbitrary but consistent with the data and our state of belief about the system. As we will see, the large uncertainties in N_{proto} will manifest themselves as a broad spread in protostellar lifetimes.

The probability distribution for the age of the clusters, $P(A)$ we take as a simple Gaussian, mean 3.5 Myr, standard deviation

0.5 Myr. The probability of the number of pre-main-sequence stars, $P(N_{\text{PMS}})$, is also a Gaussian given by the product of the 536 ± 53 stars identified in NGC1333 and IC348 and a factor representing the $43\% \pm 20\%$ additional distributed population. The resulting distribution is also Gaussian with a mean of 652 and a standard deviation of 97. From these two distributions – age and number of PMS stars – we derive the corresponding distribution for the star formation rate, shown in the middle panel of Fig. 5, using the formula:

$$P(\text{SFR}) = \int_0^{\infty} P(A) P(N_{\text{PMS}} = A \times \text{SFR}) dA.$$

We then assume that the star formation rate has been constant since the onset of star formation in IC348 until the present day, and calculate the lifetime of the protostellar phase by comparing the star formation rate with the number of protostars, $\tau_{\text{proto}} = N_{\text{proto}}/\text{SFR}$. The corresponding probability distribution,

$$P(\tau_{\text{proto}}) = \int_0^{\infty} P(N_{\text{proto}}) P(\text{SFR} = N_{\text{proto}}/\tau_{\text{proto}}) dN_{\text{proto}},$$

is shown in the bottom panel of Fig. 5.

The result is that the most probable lifetime is 0.43 Myr with 95% confidence limits of 0.25 – 0.67 Myr. The distribution is not Gaussian but skewed towards longer lifetimes, reflecting the tail of probability towards high numbers of protostars. There is a large range of lifetimes with high probabilities within the 95% confidence limits. The 95% confidence range interval is much more robust against changes in the details of the probability distribution than the position of the peak probability.

The uncertain submm detection rate for protostars and the uncertain multiplicity in the submm cores contribute the majority of the $\sim 40\%$ uncertainties in the protostellar lifetime. This will to a large extent be addressed by the next generation of more sensitive submm surveys, which have an order of magnitude better mass sensitivity and will therefore detect envelopes down to below the substellar mass limit. Sensitive mid-infrared, outflow or radio observations will be required to determine if such low-mass objects are indeed protostars. The uncertain age spreads in IC348 and NGC1333 and the uncertain count of recent (< 4 Myr) T Tauri stars outside these main clusters also contribute to the uncertainties. Much recent work has been done on age spreads in PMS clusters (Hartmann 2001; Burningham et al. 2005) and these are unlikely to improve significantly but a better count of the distributed population may come from wide-field surveys.

An embedded phase lifetime of 0.25–0.67 Myr (95% confidence limits) is consistent with the simple lower limit (0.25 Myr) we calculated at the beginning of this section but somewhat longer than the previous estimates of 0.2 ± 0.1 Myr in Rho Oph (Wilking et al. 1989; Greene et al. 1994) and 0.15 ± 0.05 Myr in Taurus-Auriga (Kenyon et al. 1990; Kenyon & Hartmann 1995). Unlike these mid-infrared based studies, we are comparing with both a larger sample of T Tauri stars, due to more sensitive photometry, and a much more complete sample of embedded stars, which includes Class 0 objects to which the earlier surveys were blind, so it is unsurprising that we reach a different conclusion.

6. Summary and conclusions

The Perseus molecular cloud is a well known site of star formation containing a population of pre-main-sequence stars similar to Ophiuchus and intermediate between Taurus and Orion

(Luhman & Rieke 1999; Briceño et al. 2002; Luhman et al. 2003). We have compiled spectral energy distributions from the near-IR to mm wavelengths (using data from Bolocam, SCUBA, IRAS, Spitzer, Michelle (where available) and 2MASS) for the 103 known submm cores across the molecular cloud. These cores lie within the boundaries of our SCUBA map of the Perseus molecular cloud, which covers roughly the area with ^{13}CO integrated intensity greater than 4 K km s^{-1} or $A_{\nu} > 4$ (Paper I). From the presence of a near- and/or mid-infrared source or molecular outflow, we have identified 56 cores which are definitely protostellar. A further 11 Class I sources have been identified by Spitzer, bringing the total number of definite protostars in Perseus to 67. There may be further protostars among our submm detections which are not yet luminous enough to be detected in the IR or be identified by their outflow activity (Paper III).

We use three evolutionary indicators to classify the sources on the basis of their spectral energy distributions: T_{bol} , $F_{3.6}/F_{850}$ and $L_{\text{submm}}/L_{\text{bol}}$. On the basis of these indicators, 22 protostars are Class I (33 including additional Spitzer-only detections) and 34 are Class 0. This is a much higher fraction of Class 0 sources than is found in Ophiuchus or Taurus. On the basis of these counts, the lifetimes for the Class 0 phase are similar to the Class I phase, rather than much shorter as has been previously found.

Protostellar envelopes in Perseus are more massive than those in Ophiuchus or Taurus and this is the main reason for the high number of Class 0-classified sources in Perseus. It is generally true that higher mass envelopes have higher optical depth envelopes and therefore SEDs which peak at longer wavelengths, resulting in lower T_{bol} . We have demonstrated this by modelling a typical Class 0 geometry at a range of different masses and find that the bolometric temperature rises as the mass decreases so that a source which would be classified Class 0 at $1 M_{\odot}$ would be classified Class I below $0.2 M_{\odot}$ on the basis of this evolutionary indicator. Low envelope mass sources, such as the majority in Taurus or Ophiuchus, are therefore more likely to be classified Class I whereas the higher mass envelopes which are detected in Perseus are more likely to be classified as Class 0. This classification issue arises because of the difficulty in defining the Class 0/Class I boundary in terms of observable evolutionary indicators, all of which (T_{bol} , $L_{\text{bol}}/L_{\text{submm}}$, $F_{3.6}/F_{850}$) vary with envelope mass for the same geometry of source. More investigation with radiative transfer models is needed to determine where the boundary should lie. However, despite the issues in classification we believe that the count of Class 0 sources in Perseus is roughly correct and similar to the number of Class Is, and that therefore – assuming a constant star formation rate – the lifetimes of these two phases, at least for stars starting from envelopes of half a solar mass or more, are similar.

There is also a possible physical explanation for why massive clusters might contain more Class 0 sources. If there is competitive accretion for material within the cloud, then more massive sources may continue to accrete material onto their envelopes and maintain their Class 0 status for longer. It is possible that this mechanism operates to maintain the Class 0 sources in Perseus and that this is why there are so many in the clustered environments.

We find that bolometric luminosity and envelope mass are roughly correlated with $\log_{10}(L_{\text{bol}}/L_{\odot}) \propto \log_{10}(M_{\text{env}}/M_{\odot})^{1.96 \pm 0.36}$, consistent with the results for Herbig-Haro flows (Reipurth et al. 1993) and the protostellar models of Smith (2000). Class 0 sources and Class I sources follow

approximately the same power law but the Class 0 sources have, on average, an order of magnitude lower luminosities.

Our estimate for the lifetime of the entire embedded protostellar phase is 0.25–0.67 Myr. This estimate, higher than previous estimates of ~ 0.2 Myr, is based on our survey of protostars with corrections for multiplicity and incompleteness, and with counts and age estimates for T Tauri stars from recent censuses of the populations in IC348 and NGC1333, assuming a constant star formation rate in Perseus over the last 3.5 ± 0.5 Myr.

The ratio of starless cores above the submm detection limit to protostars in Perseus is at most 0.8, though this could reduce as apparently starless cores may yet be identified as protostellar by more sensitive IR or outflow observations. The lifetime for a detectable starless core ($> 0.3 M_{\odot}$ within one SCUBA beam) is therefore at least 0.8 times the protostellar lifetime or 0.4 Myr.

Acknowledgements. The James Clerk Maxwell Telescope is operated by the Joint Astronomy Centre on behalf of the Particle Physics and Astronomy Research Council of the United Kingdom, the Netherlands Organisation for Scientific Research, and the National Research Council of Canada. JH acknowledges support from Deutsche Forschungsgemeinschaft SFB 494 and the PPARC Advanced Fellowship programme. This research made use of the Spitzer archive operated by the Spitzer Science Centre and the SIMBAD query facility of the Centre de Données Astronomiques de Strasbourg. The authors would like to thank Tim Naylor and Nathan Mayne for useful discussions on the ages of IC348 and NGC1333, and the referee for comments which substantially improved the clarity of the discussion.

References

- Allen, L., Myers, P., Wolk, S., et al. in prep., in prep.
 Andre, P. & Montmerle, T. 1994, *ApJ*, 420, 837
 Andre, P., Ward-Thompson, D., & Barsony, M. 1993, *ApJ*, 406, 122
 Anglada, G. & Rodríguez, L. F. 2002, *Revista Mexicana de Astronomía y Astrofísica*, 38, 13
 Anglada, G., Rodríguez, L. F., & Torrelles, J. M. 2000, *ApJ*, 542, L123
 Arce, H. G. & Sargent, A. I. 2006, *ApJ*, 646, 1070
 Aspin, C. 2003, *AJ*, 125, 1480
 Aspin, C., Sandell, G., & Russell, A. P. G. 1994, *A&AS*, 106, 165
 Avila, R., Rodríguez, L. F., & Curiel, S. 2001, *Revista Mexicana de Astronomía y Astrofísica*, 37, 201
 Bachiller, R., Andre, P., & Cabrit, S. 1991, *A&A*, 241, L43
 Bachiller, R. & Cernicharo, J. 1986, *A&A*, 168, 262
 Barnard, V. E., Vielva, P., Pierce-Price, D. P. I., et al. 2004, *MNRAS*, 352, 961
 Barsony, M., Ward-Thompson, D., André, P., & O’Linger, J. 1998, *ApJ*, 509, 733
 Bate, M. R., Bonnell, I. A., & Bromm, V. 2003, *MNRAS*, 339, 577
 Bertin, E. & Arnouts, S. 1996, *A&AS*, 117, 393
 Bonnell, I. A. & Bate, M. R. 2006, *MNRAS*, 624
 Bonnell, I. A., Bate, M. R., Clarke, C. J., & Pringle, J. E. 2001, *MNRAS*, 323, 785
 Bontemps, S., Andre, P., Terebey, S., & Cabrit, S. 1996, *A&A*, 311, 858
 Briceño, C., Luhman, K. L., Hartmann, L., Stauffer, J. R., & Kirkpatrick, J. D. 2002, *ApJ*, 580, 317
 Burningham, B., Naylor, T., Littlefair, S. P., & Jeffries, R. D. 2005, *MNRAS*, 363, 1389
 Carpenter, J. M. 2000, *AJ*, 120, 3139
 Chandler, C. J. & Richer, J. S. 2000, *ApJ*, 530, 851
 Chen, H., Myers, P. C., Ladd, E. F., & Wood, D. O. S. 1995, *ApJ*, 445, 377
 Chini, R., Reipurth, B., Sievers, A., et al. 1997a, *A&A*, 325, 542
 Chini, R., Reipurth, B., Sievers, A., et al. 1997b, *A&A*, 325, 542
 Curiel, S., Raymond, J. C., Moran, J. M., Rodríguez, L. F., & Canto, J. 1990, *ApJ*, 365, L85
 de Zeeuw, P. T., Hoogerwerf, R., de Bruijne, J. H. J., Brown, A. G. A., & Blaauw, A. 1999, *AJ*, 117, 354
 de Zeeuw, T. & Brand, J. 1985, in *ASSL Vol. 120: Birth and Evolution of Massive Stars and Stellar Groups*, ed. W. Boland & H. van Woerden, 95–101
 Dent, W. R. F., Mathews, H. E., & Ward-Thompson, D. 1998, *MNRAS*, 301, 1049
 Draine, B. T. & Lee, H. M. 1984, *ApJ*, 285, 89
 Draine, B. T. & Malhotra, S. 1993, *ApJ*, 414, 632
 Duchêne, G., Bouvier, J., & Simon, T. 1999, *A&A*, 343, 831
 Duquennoy, A. & Mayor, M. 1991, *A&A*, 248, 485
 Dutrey, A., Guilloteau, S., & Bachiller, R. 1997, *A&A*, 325, 758

- Eisloffel, J., Froebrich, D., Stanke, T., & McCaughrean, M. J. 2003, *ApJ*, 595, 259
- Enoch, M. L., Young, K. E., Glenn, J., et al. 2006, *ApJ*, 638, 293
- Evans, N. J., Allen, L. E., Blake, G. A., et al. 2003, *PASP*, 115, 965
- Froebrich, D. 2005, *ApJS*, 156, 169
- Gimenez, A. & Clausen, J. V. 1994, *A&A*, 291, 795
- Greene, T. P., Wilking, B. A., Andre, P., Young, E. T., & Lada, C. J. 1994, *ApJ*, 434, 614
- Harries, T. J. 2000, *MNRAS*, 315, 722
- Harries, T. J., Monnier, J. D., Symington, N. H., & Kurosawa, R. 2004, *MNRAS*, 350, 565
- Hartigan, P., Heathcote, S., Morse, J. A., Reipurth, B., & Bally, J. 2005, *AJ*, 130, 2197
- Hartmann, L. 2001, *AJ*, 121, 1030
- Hatchell, J., Richer, J., & Fuller, G. 2006, in prep. (Paper III)
- Hatchell, J., Richer, J. S., Fuller, G. A., et al. 2005, *A&A*, 440, 151, (Paper I)
- Henriksen, R., Andre, P., & Bontemps, S. 1997, *A&A*, 323, 549
- Hirano, N., Kamazaki, T., Mikami, H., Ohashi, N., & Umemoto, T. 1999a, in *Star Formation 1999, Proceedings of Star Formation 1999*, held in Nagoya, Japan, June 21 - 25, 1999, Editor: T. Nakamoto, Nobeyama Radio Observatory, p. 181-182, 181-182
- Hirano, N., Kamazaki, T., Mikami, H., Ohashi, N., & Umemoto, T. 1999b, in *Star Formation 1999, Proceedings of Star Formation 1999*, held in Nagoya, Japan, June 21 - 25, 1999, Editor: T. Nakamoto, Nobeyama Radio Observatory, p. 181-182, ed. T. Nakamoto, 181-182
- Hirano, N., Liu, S.-Y., Shang, H., et al. 2006, *ApJ*, 636, L141
- Hurt, R. L. & Barsony, M. 1996, *ApJ*, 460, L45+
- Indebetouw, R., Whitney, B. A., Johnson, K. E., & Wood, K. 2006, *ApJ*, 636, 362
- Ivezic, Z. & Elitzur, M. 1997, *MNRAS*, 287, 799
- Jennings, R. E., Cameron, D. H. M., Cudlip, W., & Hirst, C. J. 1987, *MNRAS*, 226, 461
- Jessop, N. E. & Ward-Thompson, D. 2000, *MNRAS*, 311, 63
- Johnstone, D., Wilson, C. D., Moriarty-Schieven, G., Giannakopoulou-Creighton, J., & Gregersen, E. 2000, *ApJS*, 131, 505
- Jørgensen, J. K., Harvey, P. M., Evans, II, N. J., et al. 2006, *ApJ*, 645, 1246
- Jørgensen, J. K., Johnstone, D., Kirk, H., & Myers, P. in prep., in prep.
- Kaas, A. A., Olofsson, G., Bontemps, S., et al. 2004, *A&A*, 421, 623
- Kenyon, S. J. & Hartmann, L. 1995, *ApJS*, 101, 117
- Kenyon, S. J., Hartmann, L. W., Strom, K. M., & Strom, S. E. 1990, *AJ*, 99, 869
- Kirk, H., Johnstone, D., & Di Francesco, J. 2006, *ApJ*, 646, 1009
- Kurosawa, R., Harries, T. J., Bate, M. R., & Symington, N. H. 2004, *MNRAS*, 351, 1134
- Lada, C. J., Alves, J., & Lada, E. A. 1996, *AJ*, 111, 1964
- Ladd, E. F., Myers, P. C., & Goodman, A. A. 1994, *ApJ*, 433, 117
- Lay, O. P., Carlstrom, J. E., & Hills, R. E. 1995, *ApJ*, 452, L73+
- Lee, C. W. & Myers, P. C. 1999, *ApJS*, 123, 233
- Looney, L. W., Mundy, L. G., & Welch, W. J. 2000, *ApJ*, 529, 477
- Lucy, L. B. 1999, *A&A*, 344, 282
- Luhman, K. L. & Rieke, G. H. 1999, *ApJ*, 525, 440
- Luhman, K. L., Rieke, G. H., Lada, C. J., & Lada, E. A. 1998, *ApJ*, 508, 347
- Luhman, K. L., Stauffer, J. R., Muench, A. A., et al. 2003, *ApJ*, 593, 1093
- Magakian, T. Y. 2003, *A&A*, 399, 141
- Mathis, J. S., Rimpl, W., & Nordsieck, K. H. 1977, *ApJ*, 217, 425
- Mayne, N., Naylor, T., Littlefair, S., Saunders, E., & Jeffries, R. in prep., in prep.
- McCaughrean, M. J., Rayner, J. T., & Zinnecker, H. 1994, *ApJ*, 436, L189
- Megeath, T. & al. 2006, *astro-ph/0507552*
- Motte, F. & André, P. 2001, *A&A*, 365, 440
- Motte, F., André, P., & Neri, R. 1998, *A&A*, 336, 150
- Muench, A. A., Lada, E. A., Lada, C. J., et al. 2003, *AJ*, 125, 2029
- Myers, P. C. & Ladd, E. F. 1993, *ApJ*, 413, L47
- O'Linger, J., Wolf-Chase, G., Barsony, M., & Ward-Thompson, D. 1999, *ApJ*, 515, 696
- O'Linger, J. C., Cole, D. M., Ressler, M. E., & Wolf-Chase, G. 2006, *AJ*, 131, 2601
- Ossenkopf, V. & Henning, T. 1994, *A&A*, 291, 943
- Preibisch, T. & Zinnecker, H. 2001, *AJ*, 122, 866
- Reipurth, B., Chini, R., Krugel, E., Kreysa, E., & Sievers, A. 1993, *A&A*, 273, 221
- Rengel, M., Froebrich, D., Hodapp, K., & Eisloffel, J. 2002, in *The Origins of Stars and Planets: The VLT View*, ed. J. Alves & M. McCaughrean
- Rodríguez, L. F., Anglada, G., & Curiel, S. 1997, *ApJ*, 480, L125+
- Rodríguez, L. F., Anglada, G., & Curiel, S. 1999, *ApJS*, 125, 427
- Rodríguez, L. F. & Reipurth, B. 1998, *Revista Mexicana de Astronomia y Astrofisica*, 34, 13
- Sandell, G. & Knee, L. B. G. 2001, *ApJ*, 546, L49
- Schmeja, S. & Klessen, R. S. 2004, *A&A*, 419, 405
- Shakura, N. I. & Sunyaev, R. A. 1973, *A&A*, 24, 337
- Shirley, Y. L., Evans, II, N. J., & Rawlings, J. M. C. 2002, *ApJ*, 575, 337
- Slesnick, C. L., Carpenter, J. M., Hillenbrand, L. A., & Mamajek, E. E. 2006, *AJ*, 132, 2665
- Smith, M. D. 2000, *Irish Astronomical Journal*, 27, 25
- Snell, R. L. & Bally, J. 1986, *ApJ*, 303, 683
- Stamatellos, D., Whitworth, A. P., Boyd, D. F. A., & Goodwin, S. P. 2005, *A&A*, 439, 159
- Strom, S. E., Vrba, F. J., & Strom, K. M. 1976, *AJ*, 81, 314
- Tapia, M., Persi, P., Bohigas, J., & Ferrari-Toniolo, M. 1997, *AJ*, 113, 1769
- Tassis, K. & Mouschovias, T. C. 2004, *ApJ*, 616, 283
- Ulrich, R. K. 1976, *ApJ*, 210, 377
- Černis, K. & Straizys, V. 2003, *Baltic Astronomy*, 12, 301
- Visser, A. E., Richer, J. S., & Chandler, C. J. 2002, *AJ*, 124, 2756
- von Hippel, T., Bell Burnell, S. J., & Williams, P. M. 1988, *A&AS*, 74, 431
- Walawender, J., Bally, J., Kirk, H., & Johnstone, D. 2005, *AJ*, 130, 1795
- Ward-Thompson, D., Scott, P. F., Hills, R. E., & Andre, P. 1994, *MNRAS*, 268, 276
- Whitney, B. A., Wood, K., Bjorkman, J. E., & Cohen, M. 2003, *ApJ*, 598, 1079
- Whitworth, A. P. & Ward-Thompson, D. 2001, *ApJ*, 547, 317
- Wilking, B. A., Lada, C. J., & Young, E. T. 1989, *ApJ*, 340, 823
- Wilking, B. A., Meyer, M. R., Greene, T. P., Mikhail, A., & Carlson, G. 2004, *AJ*, 127, 1131
- Williams, J. P., de Geus, E. J., & Blitz, L. 1994, *ApJ*, 428, 693
- Wolf-Chase, G. A., Barsony, M., & O'Linger, J. 2000, *AJ*, 120, 1467
- Young, C. H., Shirley, Y. L., Evans, II, N. J., & Rawlings, J. M. C. 2003, *ApJS*, 145, 111

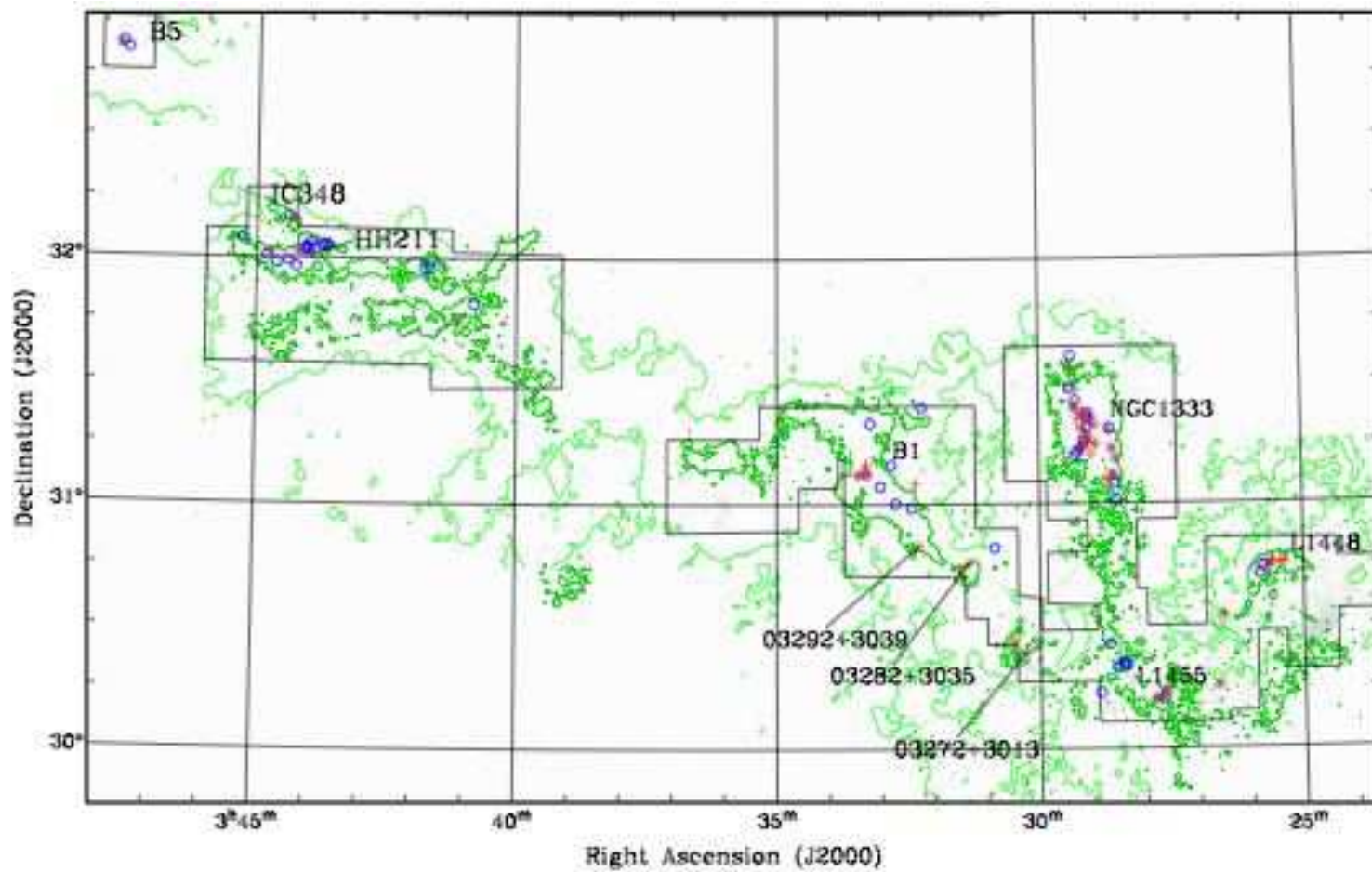


Fig. 6. Class 0 (red crosses), Class I (maroon stars) and starless cores (blue circles) overlaid on the Perseus molecular cloud outlined in C¹⁸O (dark green contours 1 K km s⁻¹, Hatchell et al. (2005)) and ¹³CO (light green contours 3 K km s⁻¹, Bell Labs 7m survey made available by John Bally [http://casa/colorado.edu/~bally](http://casa.colorado.edu/~bally)). The area mapped by SCUBA is marked.

Online Material

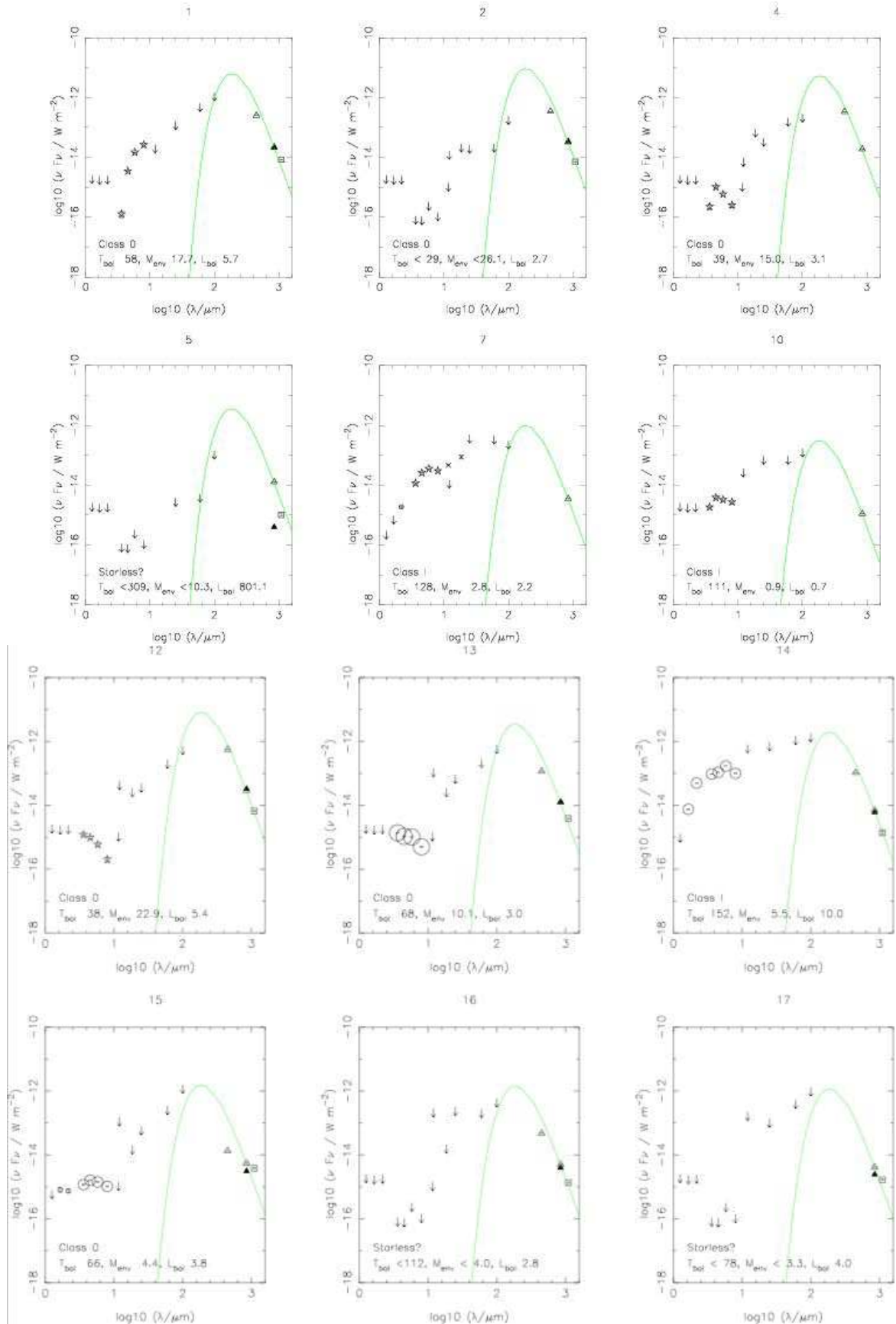


Fig. 7. Spectral energy distributions for the 103 submm detections in Perseus. Contributions from short to long wavelength: 2MASS (circles), Spitzer IRAC (stars), Michelle (x), IRAS HIRES (arrows), SCUBA (open triangles - Clumpfind; filled triangles - 90'' diameter aperture), Bolocam (squares). Upper limits (including IRAS HIRES) are marked as arrows and large circles denote more than one association. A 10 K greybody passing through the 850 μm flux point is overplotted (green).

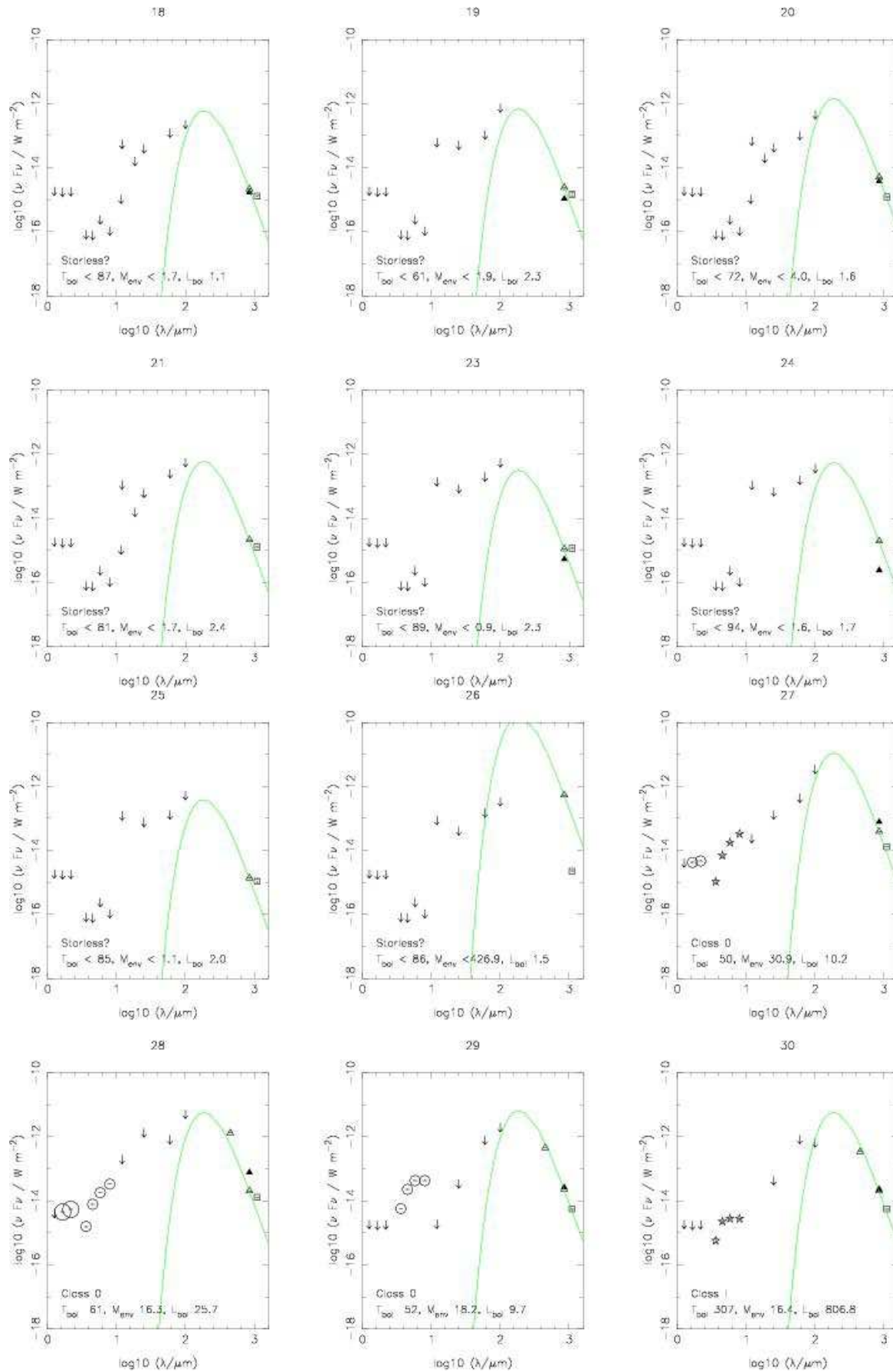


Fig. 7. Continued.

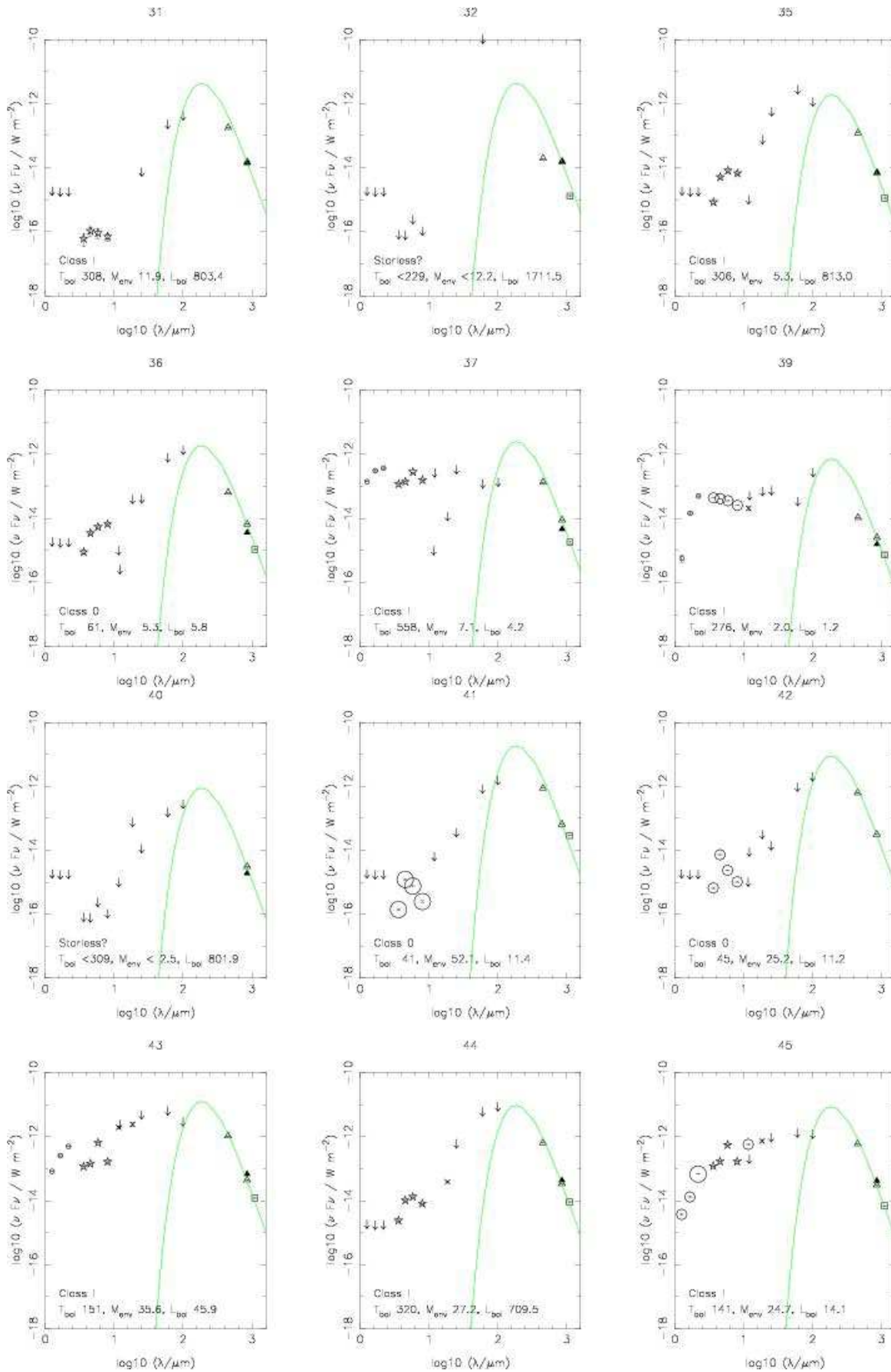


Fig. 7. Continued.

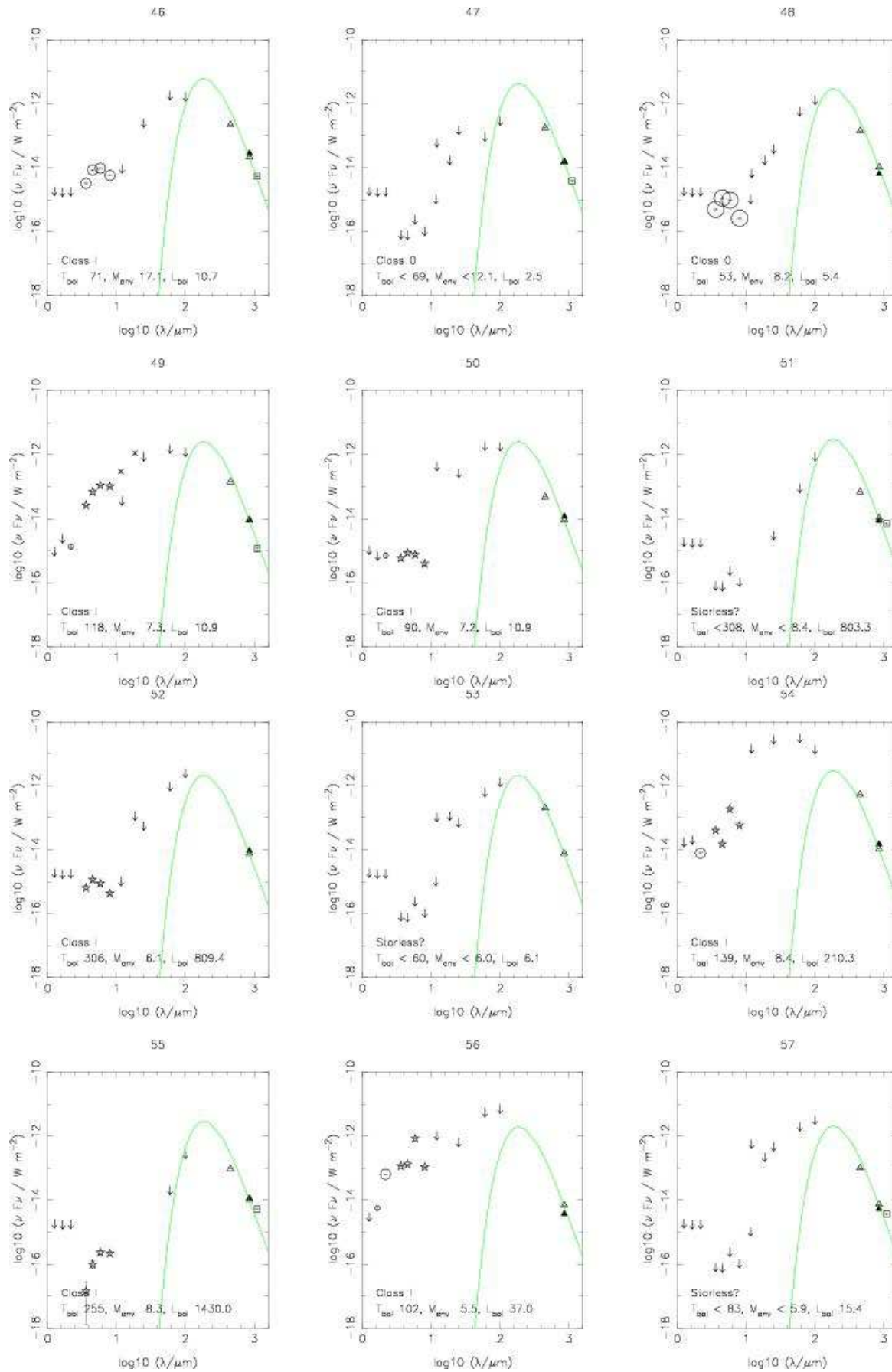


Fig. 7. Continued.

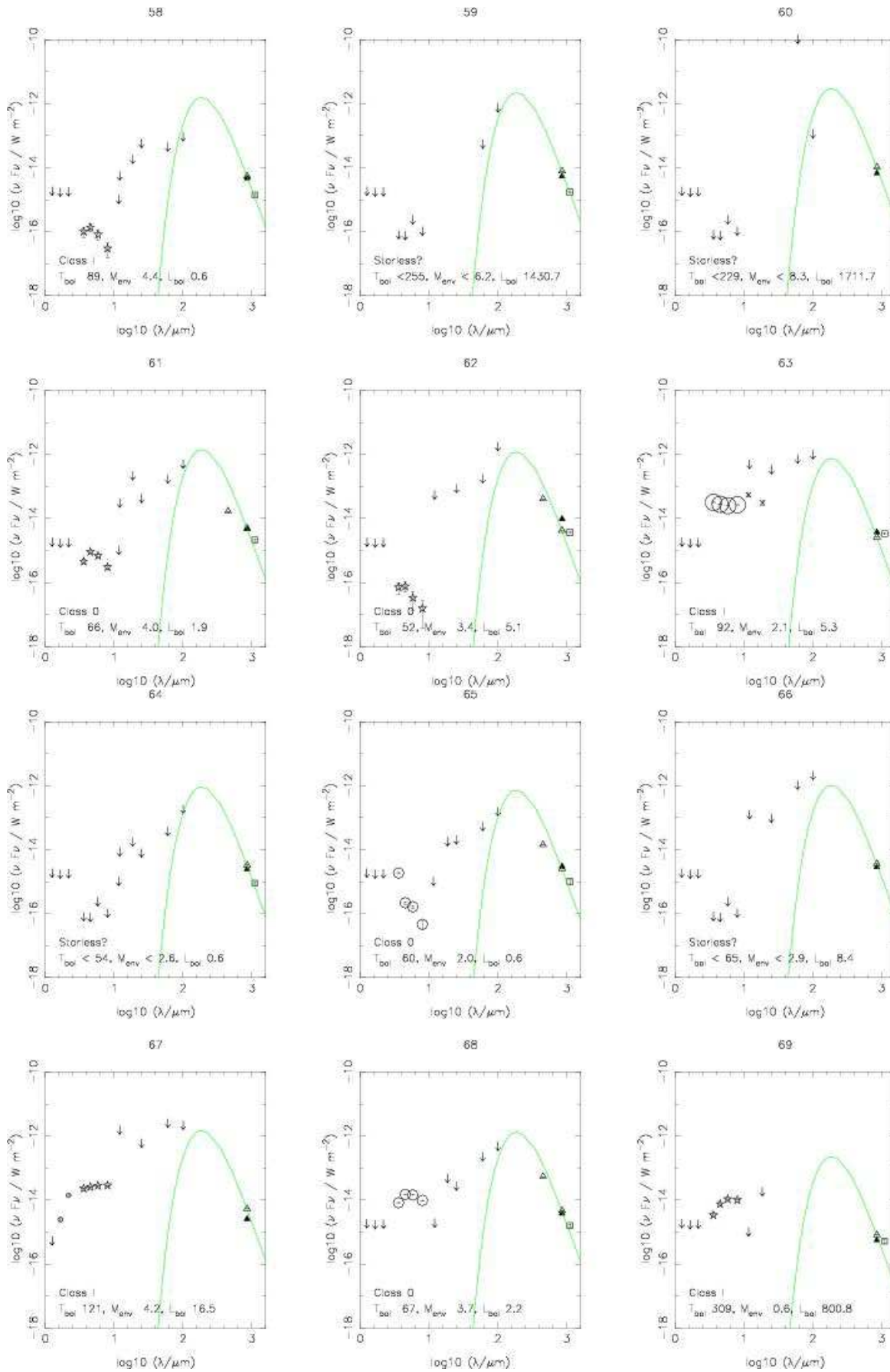


Fig. 7. Continued.

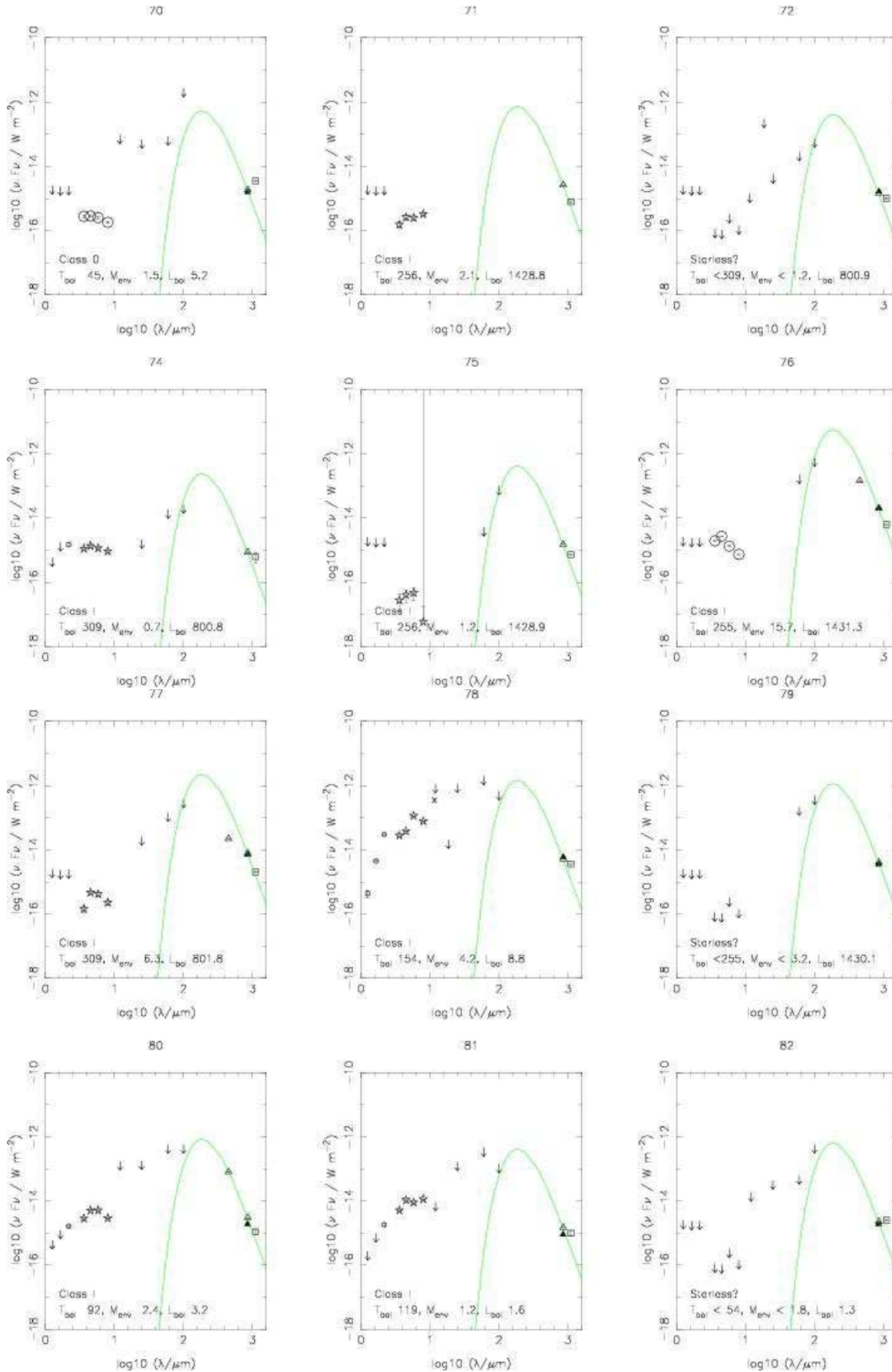


Fig. 7. Continued.

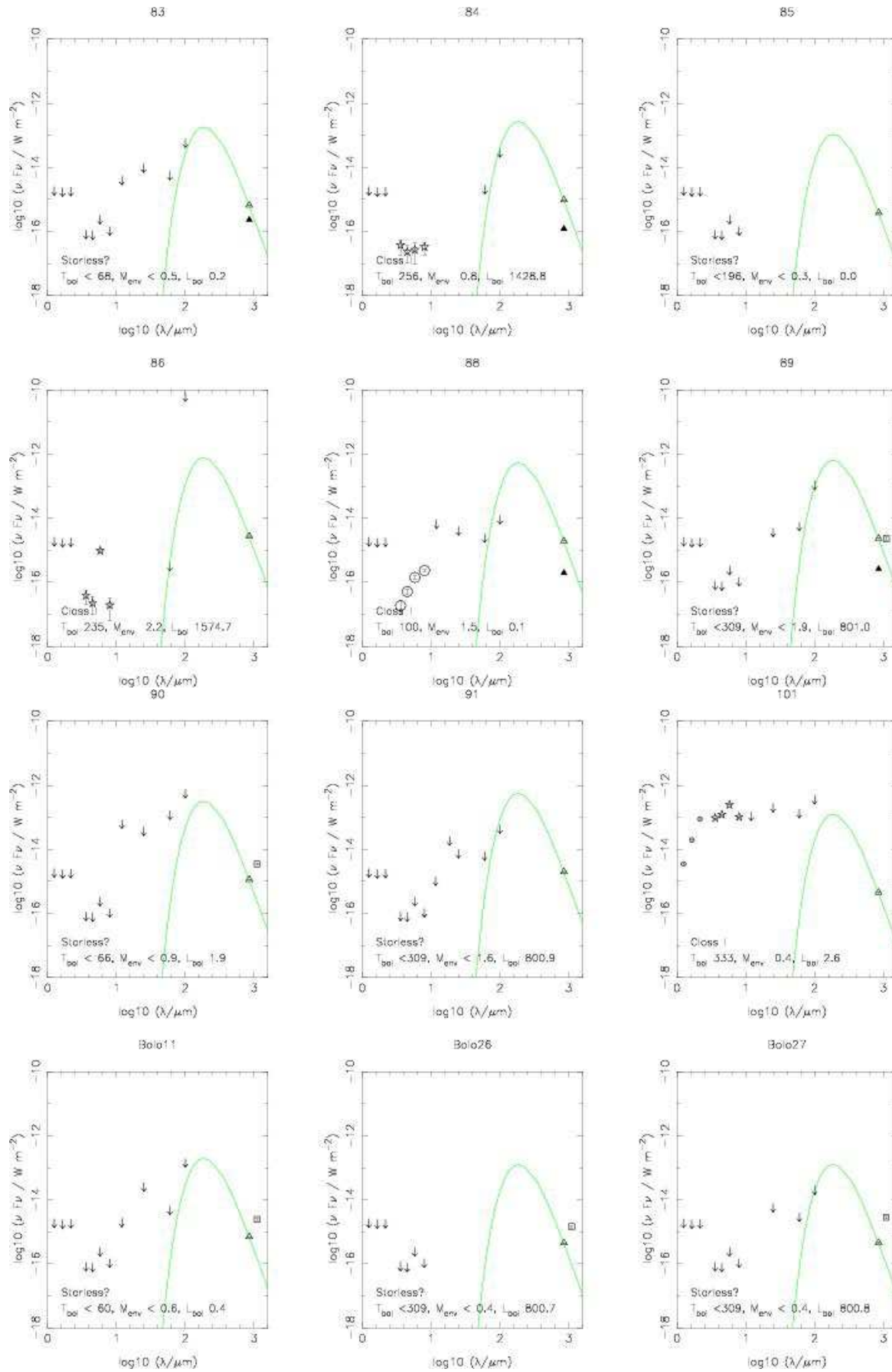


Fig. 7. Continued.

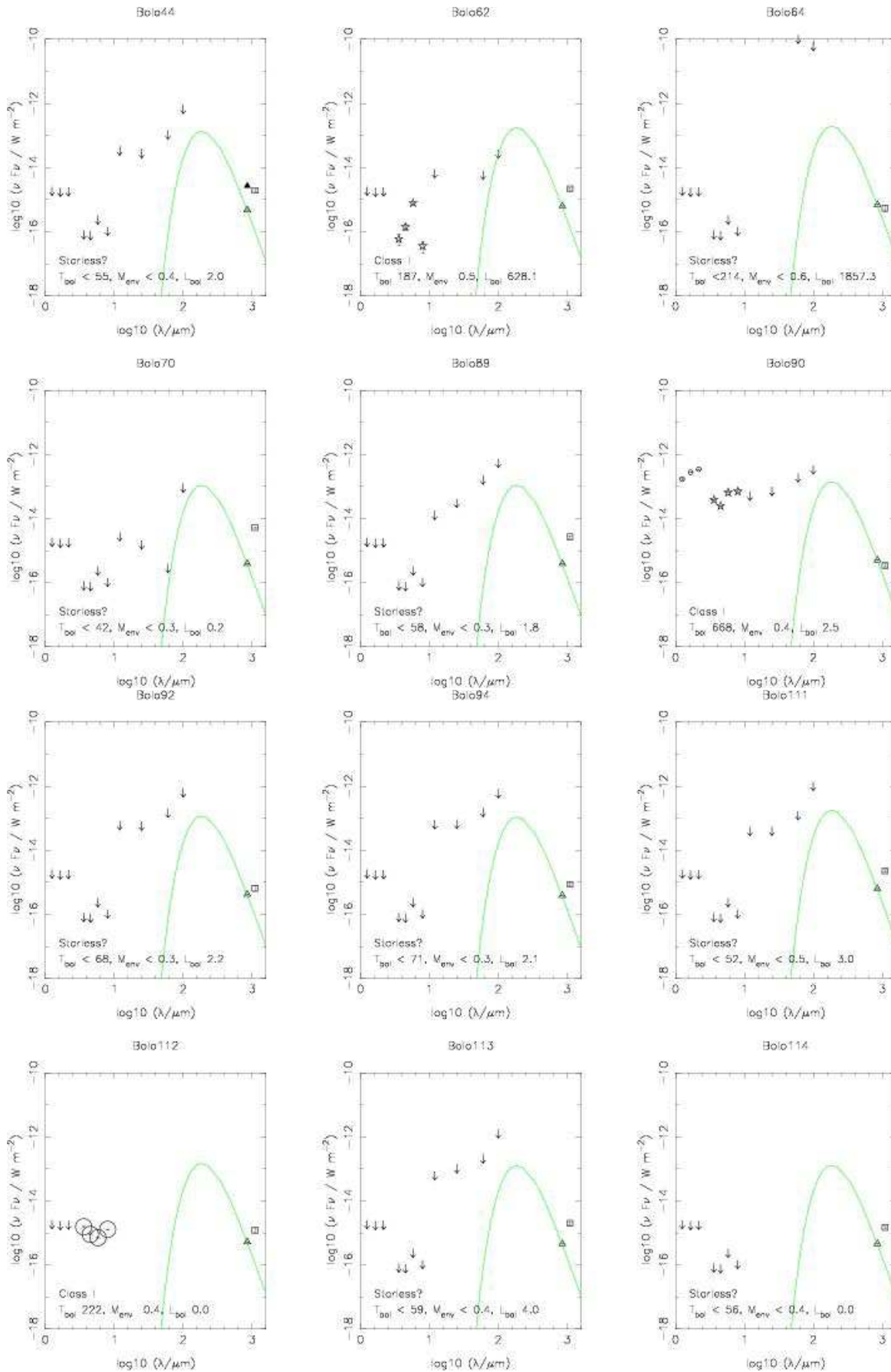
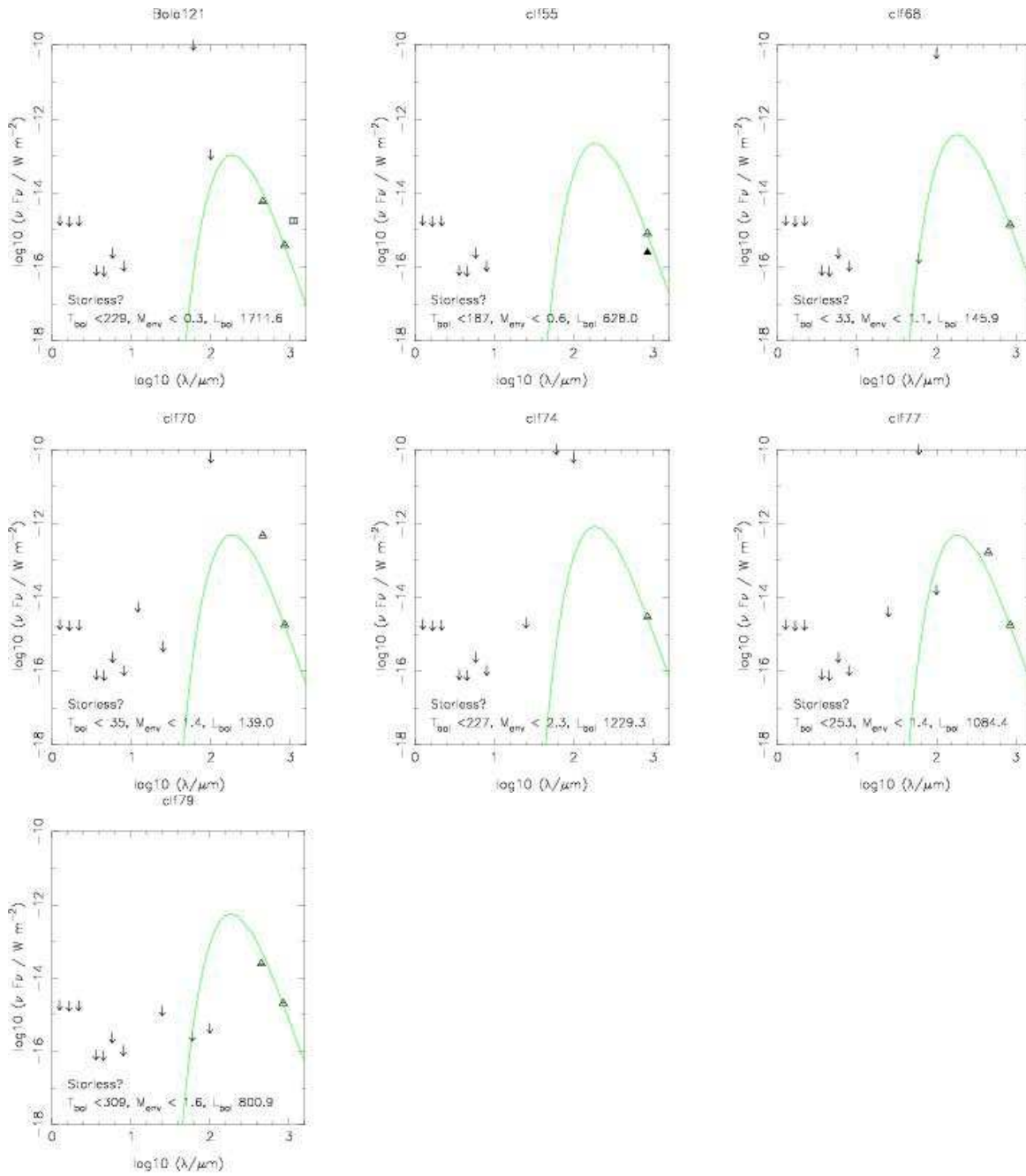


Fig. 7. Continued.



name: 3-fig-008.tif

Fig. 7. Continued.

Table 4. Source properties: integrated 850 μ m flux F_{850} ; integrated 450 μ m flux F_{450} ; bolometric luminosity L_{bol} ; envelope mass M_{env} calculated at 10 K; the three evolutionary indicators – bolometric temperature T_{bol} ; $L_{\text{smm}}/L_{\text{bol}}$; and $F_{3.6}/F_{850}$ (the number in brackets is the power of ten); and classification. Sources are classed as starless (S) if there is no infrared source or outflow, otherwise the classification is based on the three evolutionary indicators discussed in Sect.3, which, giving the condition for a Class I are: $T_{\text{bol}} > 70$ K; $L_{\text{bol}}/L_{\text{smm}} > 3000$; and $F_{3.6}/F_{850} > 0.003$. The final classification is based on the majority of the indicators with results of individual indicators given in brackets in the order listed here. The commonly used source name is given in the last column; see 5 for alternative names and references.

Source	F_{850} Jy	F_{450} Jy	L_{bol} L_{\odot}	M_{env} M_{\odot}	T_{bol} K	$L_{\text{bol}}/L_{\text{smm}}$ $\times 1/3000$	$F_{3.6}/F_{850}$	Class	Name
1	6.31	37.8	3.7	17.7	53	0.5	2.4(-5)	0 (000)	b1-c
2	9.31	52.2	< 2.5	26.1	< 25	< 0.2	< 1.0(-5)	0 (000)	b1-bS
4	5.37	50.4	2.6	15.0	32	0.4	5.1(-5)	0 (000)	b1-d
5	3.67	-	< 0.3	10.3	< 33	< 0.1	< 2.6(-5)	S	
7	1.00	-	1.3	2.8	158	1.2	1.4(-2)	I (III)	IRAS 03301+3057, B1 SMM6
10	0.32	-	0.4	0.9	117	1.1	7.0(-3)	I (III)	B1 SMM11
12	8.19	83.3	4.5	22.9	31	0.5	1.8(-4)	0 (000)	HH211
13	3.59	17.6	1.9	10.1	59	0.5	4.6(-4)	0 (000)	IC348 MMS
14	1.98	15.9	5.6	5.5	180	2.6	5.8(-2)	I (III)	
15	1.57	2.0	1.9	4.4	67	1.1	9.1(-4)	0 (OIO)	
16	1.43	7.2	< 1.6	4.0	< 103	< 1.0	< 6.7(-5)	S	
17	1.18	-	< 2.0	3.3	< 78	< 1.6	< 8.1(-5)	S	
18	0.61	-	< 0.6	1.7	< 86	< 0.8	< 1.6(-4)	S	
19	0.68	-	< 1.2	1.9	< 61	< 1.6	< 1.4(-4)	S	
20	1.44	-	< 0.9	4.0	< 70	< 0.5	< 6.7(-5)	S	
21	0.62	-	< 1.2	1.7	< 81	< 1.8	< 1.6(-4)	S	
23	0.32	-	< 1.2	0.9	< 89	< 3.3	< 3.0(-4)	S	
24	0.56	-	< 0.9	1.6	< 93	< 1.4	< 1.7(-4)	S	
25	0.39	-	< 1.0	1.1	< 85	< 2.4	< 2.5(-4)	S	
26	152.43	-	< 0.8	2.7	< 84	< 0.7	< 1.0(-4)	S	
27	11.03	-	5.4	30.9	53	0.5	1.1(-4)	0 (000)	L1448 NW
28	5.83	196.9	17.0	16.3	53	2.7	3.3(-4)	0 (OIO)	L1448 N A/B
29	6.51	68.4	6.3	18.2	49	0.9	1.1(-3)	0 (000)	L1448C
30	5.85	51.1	4.1	16.4	50	0.7	1.2(-4)	0 (000)	L1448 IRS2
31	4.26	26.5	1.9	11.9	38	0.4	1.7(-5)	0 (000)	
32	4.36	2.9	< 0.2	12.2	< 20	< 0.0	< 2.2(-5)	S	
35	1.89	18.4	7.0	5.3	105	3.4	5.3(-4)	I (OIO)	L1455 FIR4
36	1.91	9.8	3.1	5.3	59	1.5	5.6(-4)	0 (OIO)	
37	2.52	20.5	3.3	7.1	672	1.2	5.6(-2)	I (III)	L1455 PP9
39	0.72	1.6	0.8	2.0	394	1.0	7.3(-2)	I (OIO)	L1455 FIR1/2
40	0.89	-	< 0.6	2.5	< 63	< 0.6	< 1.1(-4)	S	
41	18.61	131.0	8.5	52.1	35	0.4	9.1(-6)	0 (000)	NGC1333 IRAS 4A
42	9.00	94.6	7.6	25.2	39	0.8	8.9(-5)	0 (000)	NGC1333 IRAS 4B
43	12.70	159.9	29.5	35.6	180	2.1	1.1(-2)	I (III)	NGC1333 SVS13
44	9.73	95.6	22.7	27.2	58	2.2	2.9(-4)	0 (OIO)	NGC1333 IRAS 2A
45	8.82	91.3	10.2	24.7	164	1.1	1.6(-2)	I (III)	NGC1333 ASR 114
46	6.10	32.8	6.1	17.1	67	0.9	6.4(-4)	0 (000)	NGC1333 ASR 32/33
47	4.33	26.3	< 1.8	12.1	< 54	< 0.4	< 2.2(-5)	0 (000)	NGC1333 SK31
48	2.92	20.9	3.2	8.2	49	1.0	2.0(-4)	0 (000)	NGC1333 IRAS 4C
49	2.59	21.1	6.8	7.3	140	2.4	1.2(-2)	I (III)	NGC1333 SK6
50	2.58	7.1	5.6	7.2	88	2.0	2.7(-4)	I (OIO)	NGC1333 HH 7-11 MMS 4
51	3.01	10.1	< 1.5	8.4	< 37	< 0.5	< 3.2(-5)	S	NGC1333 SK16
52	2.17	-	4.4	6.1	57	1.9	3.5(-4)	0 (OIO)	NGC1333 HH7-11 MMS 6
53	2.14	29.7	< 3.7	6.0	< 54	< 1.6	< 4.5(-5)	S	NGC1333 SK26
54	3.01	78.8	106.9	8.4	138	32.7	1.6(-2)	I (III)	NGC1333 SK28
55	2.96	14.4	1.0	8.3	50	0.3	5.8(-6)	0 (000)	
56	1.96	-	19.1	5.5	124	9.0	7.1(-2)	I (III)	NGC1333 SK29
57	2.10	15.1	< 8.0	5.9	< 81	< 3.5	< 4.6(-5)	S	NGC1333 SK33
58	1.56	-	0.3	4.4	82	0.2	7.8(-5)	0 (IOO)	
59	2.21	-	< 1.3	6.2	< 83	< 0.5	< 4.3(-5)	S	
60	2.95	-	< 1.2	8.3	< 215	< 0.4	< 3.3(-5)	S	
61	1.42	2.5	1.0	4.0	64	0.7	3.8(-4)	0 (000)	
62	1.21	6.1	2.7	3.4	50	2.0	7.1(-5)	0 (OIO)	NGC1333 SK18
63	0.76	-	2.8	2.1	103	3.4	5.1(-2)	I (III)	NGC1333 SK32
64	0.92	-	< 0.3	2.6	< 52	< 0.3	< 1.0(-4)	S	NGC1333 Per 4A3/4D
65	0.72	2.1	0.4	2.0	56	0.5	3.1(-3)	0 (OIO)	NGC1333 IRAS 4B1
66	1.03	-	< 4.2	2.9	< 65	< 3.8	< 9.3(-5)	S	NGC1333 SK30
67	1.51	-	8.4	4.2	127	5.1	1.8(-2)	I (III)	
68	1.34	8.2	1.3	3.7	69	0.9	7.4(-3)	0 (OIO)	
69	0.23	-	0.04	0.6	436	0.2	1.8(-2)	I (OIO)	
70	0.53	-	2.6	1.5	45	4.5	6.3(-4)	0 (OIO)	NGC1333 SK22
71	0.75	-	0.03	2.1	37	0.0	2.5(-4)	0 (000)	NGC1333 HH 340B
72	0.42	-	< 0.1	1.2	< 64	< 0.3	< 2.3(-4)	S	

Table 4. continued.

Source	F_{850} Jy	F_{450} Jy	L_{bol} L_{\odot}	M_{env} M_{\odot}	T_{bol} K	$L_{\text{bol}}/L_{\text{snn}}$ $\times 1/3000$	$F_{3.6}/F_{850}$	Class	Name ¹
74	0.24	-	0.06	0.7	144	0.2	5.4(-3)	I (IOI)	
75	0.43	-	0.1	1.2	67	0.3	7.7(-5)	0 (000)	
76	5.60	21.5	2.4	15.7	109	0.4	4.2(-4)	0 (IO0)	B1 SMM5
77	2.26	3.3	0.7	6.3	60	0.3	7.7(-5)	0 (000)	B1 SMM7
78	1.49	-	4.7	4.2	181	2.9	2.3(-2)	I (III)	B5 IRS1
79	1.16	-	< 1.4	3.2	< 175	< 1.1	< 8.3(-5)	S	
80	0.86	12.1	1.9	2.4	86	2.0	3.9(-3)	I (III)	IRAS 03235+3004
81	0.42	-	0.8	1.2	133	1.8	1.5(-2)	I (III)	IRAS 03271+3013
82	0.65	-	< 0.7	1.8	< 53	< 0.9	< 1.5(-4)	S	B1 SMM1
83	0.19	-	< 0.10	0.5	< 68	< 0.6	< 6.8(-4)	S	
84	0.28	-	0.06	0.8	74	0.2	1.6(-4)	0 (IO0)	
85	0.11	-	< 0.00	0.3	< 196	< 0.1	< 3.9(-3)	S	IRAS 03254+3050
86	0.79	-	0.06	2.2	49	0.1	5.8(-5)	0 (000)	
88	0.55	-	0.05	1.5	83	0.1	4.0(-5)	0 (IO0)	
89	0.66	-	< 0.2	1.9	< 45	< 0.2	< 1.4(-4)	S	B1 SMM9
90	0.33	-	< 0.9	0.9	< 66	< 2.7	< 2.9(-4)	S	Per 7
91	0.58	-	< 0.1	1.6	< 74	< 0.2	< 1.7(-4)	S	Per 4A
101	0.13	-	1.6	0.4	463	35.2	2.7(0)	I (III)	IRAS 03410+3152
Bolo11	0.20	-	< 0.2	0.6	< 60	< 1.0	< 4.8(-4)	S	
Bolo26	0.13	-	< 0.01	0.4	< 64	< 0.0	< 8.7(-4)	S	
Bolo27	0.13	-	< 0.05	0.4	< 103	< 0.4	< 9.4(-4)	S	
Bolo44	0.14	-	< 1.0	0.4	< 55	< 10.6	< 1.1(-3)	S	
Bolo62	0.18	-	0.07	0.5	103	0.4	4.0(-4)	0 (IO0)	
Bolo64	0.20	-	< 0.1	0.6	< 237	< 0.5	< 4.8(-4)	S	
Bolo70	0.11	-	< 0.1	0.3	< 42	< 1.7	< 1.5(-3)	S	
Bolo89	0.11	-	< 0.9	0.3	< 58	< 13.2	< 1.5(-3)	S	
Bolo90	0.14	-	1.7	0.4	943	24.9	7.3(-1)	I (III)	IRAS 03380+3135
Bolo92	0.12	-	< 1.1	0.3	< 68	< 19.2	< 1.9(-3)	S	
Bolo94	0.11	-	< 1.1	0.3	< 71	< 28.4	< 2.8(-3)	S	
Bolo111	0.18	-	< 1.5	0.5	< 52	< 7.6	< 5.3(-4)	S	
Bolo112	0.15	-	0.01	0.4	222	0.1	1.3(-2)	I (IOI)	
Bolo113	0.13	-	< 2.0	0.4	< 59	< 14.2	< 7.4(-4)	S	
Bolo114	0.13	-	< 0.01	0.4	< 56	< 0.0	< 7.2(-4)	S	
Bolo121	0.11	0.9	< 1.1	0.3	< 231	< 34.2	< 3.3(-3)	S	
clf55	0.23	-	< 0.01	0.6	< 67	< 0.0	< 7.8(-4)	S	
clf68	0.39	-	< 0.03	1.1	< 42	< 0.1	< 2.5(-4)	S	
clf70	0.51	70.2	< 5.1	1.4	< 34	< 9.3	< 1.9(-4)	S	
clf74	0.83	-	< 0.2	2.3	< 84	< 0.2	< 1.2(-4)	S	
clf77	0.50	24.5	< 1.1	1.4	< 26	< 2.0	< 1.9(-4)	S	
clf79	0.58	3.7	< 0.2	1.6	< 27	< 0.3	< 1.7(-4)	S	

Table 5. Source peak positions and cross-identification with Hatchell et al. (2005), Bolocam (Enoch et al. 2006), 2MASS, and other names commonly associated with the source.

Source	RA(J2000) h:m:s	Dec(J2000) d:':"	Paper I	Bolocam	2MASS	Other associated source names
1	03:33:17.9	31:09:33.4	1	Bolo80		b1-c (Hirano et al. 1999b), B1 SMM2 (Walawender et al. 2005)
2	03:33:21.4	31:07:30.7	2,3	Bolo81		b1-bS; b1-bN (Hirano et al. 1999b), B1 SMM1 (Walawender et al. 2005)
4	03:33:16.3	31:06:54.3	4	—		b1-d (Hirano et al. 1999b), B1 SMM3 (Walawender et al. 2005)
5	03:33:01.9	31:04:23.2	5,6,8,9,11	Bolo74		none
7	03:33:16.5	31:07:51.3	7	—	03331667+3107548	IRAS 03301+3057, B1 SMM6 (Walawender et al. 2005)
10	03:33:27.3	31:07:10.1	10	—		B1 SMM11 (Walawender et al. 2005)
12	03:43:56.5	32:00:49.9	12	Bolo103		HH211 (McCaughrean et al. 1994; Chandler & Richer 2000); HH211 VLA2 (Avila et al. 2001)
13	03:43:56.9	32:03:04.8	13	Bolo104		IC348 MMS (Eisloffel et al. 2003)
14	03:44:43.9	32:01:32.0	14	Bolo116	03444389+3201373, 03444330+3201315 03435056+3203180	none
15	03:43:50.8	32:03:24.2	15	Bolo102		none
16	03:44:01.0	32:01:54.8	16	Bolo106		none
17	03:43:57.9	32:04:01.5	17	Bolo105		none
18	03:44:03.0	32:02:24.3	18	Bolo107		CXOPZ 15 (Preibisch & Zinnecker 2001)
19	03:44:36.8	31:58:48.9	19	Bolo115		none
20	03:44:05.5	32:01:56.7	20,22	Bolo110		none
21	03:44:02.3	32:02:48.5	21	Bolo107		none
23	03:43:37.8	32:03:06.2	23	Bolo99		none
24	03:43:42.3	32:03:23.2	24	—		none
25	03:44:48.5	32:00:30.8	25	Bolo117		none
26	03:43:44.4	32:02:55.7	26	Bolo100		none
27	03:25:35.9	30:45:30.0	27,34	Bolo8	03253643+3045252	L1448 NW (Barsony et al. 1998; Bachiller & Cernicharo 1986; Curiel et al. 1990; Looney et al. 2000)
28	03:25:36.4	30:45:15.0	28,34	Bolo8	03253652+3045070, 03253643+3045252	L1448 N A/B (Barsony et al. 1998; Curiel et al. 1990; Looney et al. 2000), L1448 IRS 3A/3B (Bachiller & Cernicharo 1986), IRS2 VLA6 (Anglada & Rodríguez 2002)
29	03:25:38.8	30:44:03.6	29	Bolo10		L1448C (Barsony et al. 1998; Bachiller et al. 1991; Curiel et al. 1990)
30	03:25:22.4	30:45:10.7	30	Bolo5		IRAS 03222+3034, L1448 IRS2 (O'Linger et al. 1999), L1448 IRS2 VLA4 (Anglada & Rodríguez 2002)
31	03:25:25.9	30:45:02.7	31	—		none
32	03:25:49.0	30:42:24.6	32,33	Bolo13		none
35	03:27:39.1	30:13:00.6	35	Bolo22		IRAS 03245+3002, L1455 FIR4 (Tapia et al. 1997), RNO15 FIR (Rengel et al. 2002)
36	03:27:42.9	30:12:28.5	36	Bolo23		none
37	03:27:48.4	30:12:08.8	37,38	Bolo24	03274767+3012043	L1455 PP9 (Tapia et al. 1997), GN 03.24.7 (Magakian 2003)
39	03:27:38.1	30:13:57.3	39	Bolo21	03273825+3013585	L1455 FIR1/2 (Tapia et al. 1997)
40	03:27:39.9	30:12:09.8	40	—		none
41	03:29:10.4	31:13:30.0	41	Bolo48		NGC1333 IRAS 4A (Jennings et al. 1987), VLA25 (Rodríguez et al. 1997), SK4 (Sandell & Knee 2001)
42	03:29:12.0	31:13:10.0	42	Bolo48		NGC1333 IRAS 4B (Jennings et al. 1987), SK3 (Sandell & Knee 2001)
43	03:29:03.2	31:15:59.0	43	Bolo43	03290375+3116039	NGC1333 SVS13 (Strom et al. 1976), ASR 2 (Aspin et al. 1994), IRAS 03259+3105, HH7-11 MMS1 (Chini et al. 1997a), VLA 4a/b (Rodríguez et al. 1997)
44	03:28:55.3	31:14:36.4	44	Bolo38		NGC1333 IRAS 2A (Jennings et al. 1987)
45	03:29:01.4	31:20:28.6	45	Bolo42	03290116+3120244, 03290149+3120208, 03290051+3120284	NGC1333 ASR 114 (Aspin et al. 1994), VLA 42/43 (Rodríguez et al. 1997), SK24 (Sandell & Knee 2001)
46	03:29:11.0	31:18:27.4	46	Bolo49		NGC1333 ASR 32/33 (Aspin et al. 1994), IRAS 7 SM1/2 (Sandell & Knee 2001), VLA 2 (Snell & Bally 1986)
47	03:28:59.7	31:21:34.2	47	Bolo40		NGC1333 SK31 (Sandell & Knee 2001)
48	03:29:13.6	31:13:55.0	48	—		NGC1333 IRAS 4C (Jennings et al. 1987; Looney et al. 2000), SK5 (Sandell & Knee 2001), VLA29 (Rodríguez et al. 1999)
49	03:28:36.7	31:13:29.6	49	Bolo29	03283609+3113346	NGC1333 SK6 (Sandell & Knee 2001), IRAS 03255+3103
50	03:29:06.5	31:15:38.6	50	—	03290642+3115348	NGC1333 HH 7-11 MMS 4 (Chini et al. 1997b) ASR6 (Aspin et al. 1994), SK15 (Sandell & Knee 2001), HH8 (von Hippel et al. 1988)
51	03:29:08.8	31:15:18.1	51	Bolo46		NGC1333 SK16 (Sandell & Knee 2001)
52	03:29:03.7	31:14:53.1	52	—		NGC1333 SK14 (Sandell & Knee 2001), HH7-11 MMS 6 (Chini et al. 1997b)
53	03:29:04.5	31:20:59.1	53	—		NGC1333 SK26 (Sandell & Knee 2001)
54	03:29:10.7	31:21:45.3	54	—	03291063+3121469	NGC1333 SK28 (Sandell & Knee 2001)
55	03:28:40.4	31:17:51.3	55	Bolo31		none
56	03:29:07.7	31:21:56.8	56	—	03290773+3121575, 03290704+3121578	NGC1333 SK29 (Sandell & Knee 2001)
57	03:29:18.2	31:25:10.8	57	Bolo53		NGC1333 SK33 (Sandell & Knee 2001)

Table 5. continued.

Source	RA(J2000) h:m:s	Dec(J2000) d:':"	Paper I	Bolocam	2MASS	Other associated source names
58	03:29:24.0	31:33:20.8	58	Bolo57		none
59	03:29:16.5	31:12:34.6	59	Bolo51		none
60	03:28:39.4	31:18:27.1	60,73	—		none
61	03:29:17.3	31:27:49.6	61	Bolo52		none
62	03:29:07.1	31:17:23.7	62	Bolo45		NGC1333 SK18 (Sandell & Knee 2001)
63	03:29:18.8	31:23:16.9	63	Bolo54		NGC1333 SK32 (Sandell & Knee 2001)
64	03:29:25.5	31:28:18.1	64	Bolo58		NGC1333 Per 4A3/4D (Ladd et al. 1994)
65	03:29:00.4	31:12:01.5	65	Bolo41		NGC1333 IRAS 4B1 (Jennings et al. 1987), SK1 (Sandell & Knee 2001)
66	03:29:05.3	31:22:11.3	66	—		NGC1333 SK30 (Sandell & Knee 2001)
67	03:29:19.7	31:23:56.0	67	—	03292003+3124076	none
68	03:28:56.2	31:19:12.5	68	Bolo39		NGC1333 MBO146 (Wilking et al. 2004)
69	03:28:34.4	31:06:59.2	69	Bolo28		none
70	03:29:15.3	31:20:31.2	70	Bolo50		NGC1333 SK22 (Sandell & Knee 2001)
71	03:28:38.7	31:05:57.1	71	Bolo30		HH 340B (von Hippel et al. 1988)
72	03:29:19.1	31:11:38.1	72	Bolo55		none
74	03:28:32.5	31:11:07.7	74	Bolo25	03283258+3111040	NGC1333 38 (Lada et al. 1996)
75	03:28:42.6	31:06:10.0	75	Bolo33		none
76	03:32:17.8	30:49:46.3	76	Bolo66		IRAS 03292+3039, B1 SMM5 (Walawender et al. 2005)
77	03:31:21.0	30:45:27.8	77	Bolo65		IRAS 03282+3035, B1 SMM7 (Walawender et al. 2005)
78	03:47:41.6	32:51:44.0	78	Bolo122	03474160+3251437	IRAS03445+3242, B5 IRS1 (Motte & André 2001), HH 366 VLA 1 (Rodríguez & Reipurth 1998)
79	03:47:39.1	32:52:17.9	79	—		none
80	03:26:37.6	30:15:24.2	80	Bolo18	03263742+3015283	IRAS 03235+3004
81	03:30:15.5	30:23:42.8	81	Bolo60	03301515+3023493	IRAS 03271+3013
82	03:33:13.1	31:19:51.0	82	Bolo78		B1 SMM1 (Walawender et al. 2005)
83	03:32:48.9	31:09:40.1	83	—		none
84	03:32:21.9	31:04:55.6	84,87	—		none
85	03:28:32.5	31:00:53.0	85	—		IRAS 03254+3050 (Dent et al. 1998)
86	03:26:30.9	30:32:27.6	86	—		none
88	03:31:31.6	30:43:32.2	88	—		none
89	03:32:25.9	30:59:05.0	89	Bolo67		B1 SMM9 (Walawender et al. 2005)
90	03:45:16.5	32:04:47.1	90	Bolo119		Per 7 (Barnard et al. 2004)
91	03:29:23.3	31:36:08.6	91	—		Per 4A (Ladd et al. 1994)
101	03:44:12.8	32:01:33.9	101	—	03441297+3201354	IRAS 03410+3152
Bolo11	03:25:46.5	30:44:17.8	—	Bolo11		none
Bolo26	03:28:32.7	31:04:55.9	—	Bolo26		none
Bolo27	03:28:32.7	30:19:51.1	—	Bolo27		none
Bolo44	03:29:04.9	31:18:41.2	—	Bolo44		none
Bolo62	03:30:32.3	30:26:27.4	—	Bolo62		none
Bolo64	03:30:51.3	30:49:14.7	—	Bolo64		none
Bolo70	03:32:44.3	31:00:09.7	—	Bolo70		none
Bolo89	03:40:49.3	31:48:50.1	—	Bolo89		none
Bolo90	03:41:09.3	31:44:38.1	—	Bolo90	03410913+3144378	IRAS 03380+3135
Bolo92	03:41:40.7	31:57:59.8	—	Bolo92		none
Bolo94	03:41:46.1	31:57:22.9	—	Bolo94		none
Bolo111	03:44:14.4	31:57:57.6	—	Bolo111		none
Bolo112	03:44:15.6	32:09:15.0	—	Bolo112		CL* IC 348 LRL 329 (Luhman et al. 1998)
Bolo113	03:44:23.9	31:59:25.2	—	Bolo113		none
Bolo114	03:44:23.2	32:10:10.1	—	Bolo114		none
Bolo121	03:47:32.7	32:50:50.2	—	Bolo121		none
clf55	03:32:14.7	31:23:36.8	—	—		none
clf68	03:28:51.4	30:13:40.2	—	—		none
clf70	03:28:21.5	30:20:30.7	—	—		none
clf74	03:28:24.5	30:20:28.3	—	—		none
clf77	03:28:41.1	30:25:31.6	—	—		none
clf79	03:28:24.8	30:20:49.4	—	—		none

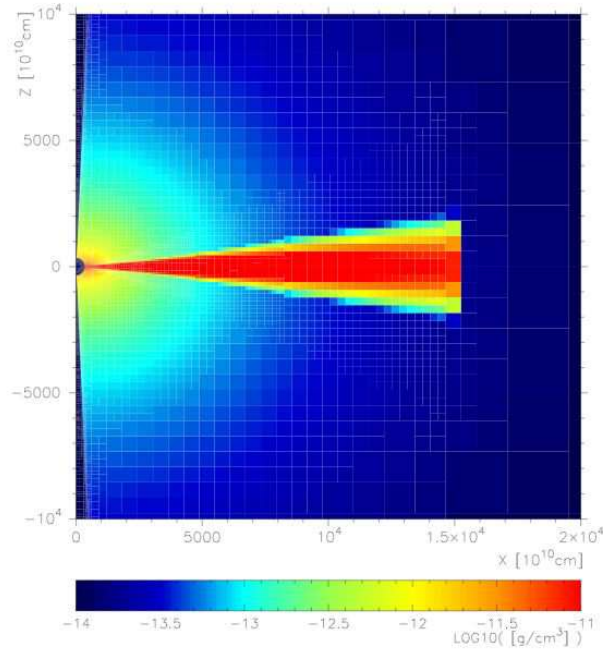


Fig. A.1. The density structure of the inner region of the Class 0 source used in the radiative-transfer modelling.

Appendix A: Class 0 models

Below we provide details of the Class 0 structure used in the radiative transfer modelling.

A.1. Density structure

We describe the geometry of the Class 0 sources using a similar density structure to that of Whitney et al. (2003). In summary, the geometry consists of a central source of mass M_* , radius R_* , and temperature $T_{\text{eff}} = 4000$ K surrounded by a canonical flared disc (Shakura & Sunyaev 1973):

$$\rho(r, z) = \rho_0 \left(\frac{R_*}{r} \right)^\alpha \exp \left(-\frac{1}{2} \left(\frac{z}{h} \right)^2 \right) \quad (\text{A.1})$$

where r is the radial distance in the midplane and z is the distance perpendicular to the midplane. The flare is imposed by a power-law dependence of the scale-height h on r : $h = h_0(r/R_*)^\beta$. The disc mass M_{disc} is then used to define ρ_0 via

$$\rho_0 = \frac{M_{\text{disc}}(\beta - \alpha + 2)}{(2\pi)^{3/2} h_0 R_*^{\alpha-\beta} (R_{\text{outer}} - R_{\text{inner}})^{\beta-\alpha+2}} \quad (\text{A.2})$$

For all the models described below we adopt the following disc parameters: $\beta = 1.25$, $\alpha = 2.25$, $h = 0.01 R_*$, $M_{\text{disc}} = 0.01 M_\odot$, $R_{\text{inner}} = 7.5 R_\odot$, and $R_{\text{outer}} = 10$ AU (Whitney et al. 2003).

The disc/star system is enshrouded by an infalling envelope of mass M_{env} , which has a density structure described by a rotationally flattened infalling envelope (Ulrich 1976):

$$\rho = \frac{\dot{M}_{\text{env}}}{4\pi} \left(\frac{GM_*}{r^3} \right)^{-1/2} \left(1 + \frac{\mu}{\mu_0} \right)^{-1/2} \left(\frac{\mu}{\mu_0} + \frac{2\mu_0^2 R_c}{r} \right)^{-1} \quad (\text{A.3})$$

where \dot{M}_{env} is the mass infall rate, R_c is the centrifugal radius, $\mu = \cos \theta = z / \sqrt{(z^2 + r^2)}$ and μ_0 is the cosine of the polar angle of a streamline of infalling material as $r \rightarrow \infty$, and is found by solving:

$$\mu_0^3 + \mu_0(r/R_c - 1) - \mu(r/R_c) = 0 \quad (\text{A.4})$$

We fix the inner radius of the envelope at R_{inner} and set the outer radius to 5000 AU. We include narrow, fixed opening angle (5°) opening angle, low density (10^{-24} g cm $^{-3}$) cavities in the polar directions. The density structure of the inner region of this Class 0 model can be seen in Figure A.1.

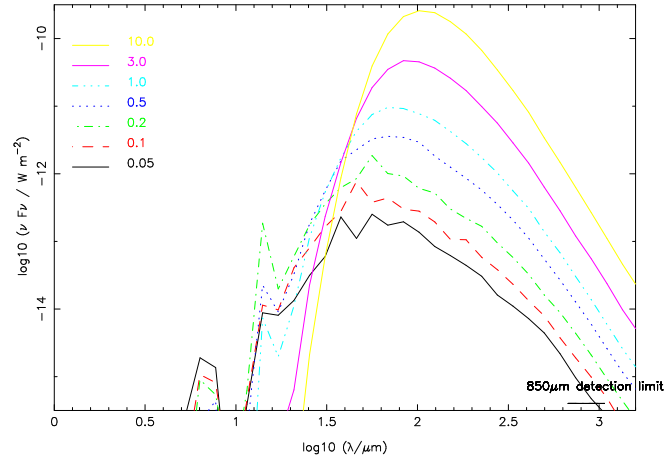


Fig. A.2. Model SEDs for Class 0 objects. The flux of the object, in λF_λ (W m^{-3}) is plotted against wavelength in microns.

Table A.1. Model parameters. The envelope mass (M_{env}), stellar mass (M_*), and stellar luminosity (L_*) are listed in solar units.

$M_{\text{env}} (M_\odot)$	$M_* (M_\odot)$	$L_* (L_\odot)$
10.00	3.33	75.9
3.00	1.00	14.9
1.00	0.33	3.4
0.50	0.17	1.3
0.20	0.07	0.38
0.10	0.03	0.15
0.05	0.02	0.06

A.2. Dust properties

We adopt a standard MRN (Mathis et al. 1977) grain-size distribution

$$n(a) da \propto a^{-3.5} da \quad (\text{A.5})$$

where $n(a)$ is the number density of grains with diameter a . We use minimum and maximum grain sizes of $0.005 \mu\text{m}$ and $1 \mu\text{m}$ respectively. We assume that the dust is composed of 62.5% ‘astronomical’ silicate and 37.5% graphite grains, with the usual 2:1 ratio of ortho- and para- graphite (Draine & Malhotra 1993). The cross-sections and Mie phase matrices were computed directly from the refractive indices tabulated by Draine & Lee (1984). A dust:gas ratio of 1:100 was used for all models.